

Fates of satellite ejecta in the Saturn system

José Luis Alvarellos^{a,*}, Kevin J. Zahnle^b, Anthony R. Dobrovolskis^c, Patrick Hamill^d

^a *Space Systems/Loral, 3825 Fabian Way, MS G-76, Palo Alto, CA 94303, USA*

^b *NASA Ames Research Center, MS 245-3, Moffett Field, CA 94035, USA*

^c *UCO/Lick Observatory, University of California, Santa Cruz, CA 95064, USA*

^d *Department of Physics, San José State University, San José, CA 95192, USA*

Received 30 November 2004; revised 8 April 2005

Available online 5 July 2005

This paper is dedicated to the memory of Richard F. Olmstead

Abstract

We use conventional numerical integrations to assess the fates of impact ejecta in the Saturn system. For specificity we consider impact ejecta launched from four giant craters on three satellites: Herschel on Mimas, Odysseus and Penelope on Tethys, and Tirawa on Rhea. Speeds, trajectories, and size of the ejecta are consistent with impact on a competent surface (“spalls”) and into unconsolidated regolith. We do not include near-field effects, jetting, or effects peculiar to highly oblique impact. Ejecta are launched at velocities comparable to or exceeding the satellite’s escape speed. Most ejecta are swept up by the source moon on time-scales of a few to several decades, and produce craters no larger than 19 km in diameter, with typical craters in the range of a few km. As much as 17% of ejecta reach satellites other than the source moon. Our models generate cratering patterns consistent with a planetocentric origin of most small impact craters on the saturnian icy moons, but the predicted craters tend to be smaller than putative Population II craters. We conclude that ejecta from the known giant craters in the saturnian system do not fully account for Population II craters.

Published by Elsevier Inc.

Keywords: Satellites of Saturn; Cratering; Impact process; Orbits

1. Introduction

Small impact craters are abundant on Saturn’s moons but it is not yet clear what formed them. This high abundance contrasts with their abundance at Jupiter. Smith et al. (1981, 1982) proposed that there were two distinct crater populations. Population I included most of the larger craters. Smith et al. attributed this population to heliocentric comets. Population II represented most of the smaller and younger craters. Compared to Population I, Population II is relatively abundant in small craters and deficient in large ones; these are also properties typical of secondary craters. Hence Smith et al. (1981, 1982, 1986) proposed that Population II was made by impact ejecta launched into planetocentric orbits about

Saturn. The resulting planetocentric debris were swept up by the many moons over the course of a few thousand years (e.g., Horedt and Neukum, 1984).

Planetocentric debris can also account for the absence of strong cratering asymmetries between the leading and trailing hemispheres. Some authors expanded on these ideas as different impactor populations were invented for different planets (see Chapman and McKinnon, 1986, and references therein). Lissauer et al. (1988), however, argued for a single impactor population, suggesting that Population I and Population II were artifacts due to crater saturation. Crater saturation is not a well-defined concept, but to a first approximation it means that on average each new crater obliterates an older one. Saturation automatically accounts for muted apex–antapex asymmetries. Lissauer et al. (1988) argued that the single impactor population is rich in small bodies. The superabundance of small impacts on an old surface produces a saturated population that has relatively

* Corresponding author. Fax: +1 650 852 5764.

E-mail address: alvarellos.jose@ssd.loral.com (J.L. Alvarellos).

fewer small craters than the production population visible on lightly cratered terrains. In support of their view they argued that craters larger than 64 km diameter on Rhea are not saturated, and that these craters implied an impactor population that was quite steep (i.e., rich in smaller bodies). If extrapolated to small sizes, this steep population could account for the abundant small craters that might otherwise be assigned to Population II.

For most of Saturn's moons, heliocentric impact velocities are high and escape speeds are low, so that a large fraction of the total ejecta is launched into orbit about Saturn. Most of the resulting planetocentric debris will strike moons to make craters. Dobrovolskis and Lissauer (2004) proposed the term 'poltorary' for this class of secondary crater. A key issue is whether poltorary craters are big enough to account for Population II. In earlier work some of us investigated the sources and orbital dynamics of material responsible for cratering Jupiter's moons (Zahnle et al., 1998, 2001, 2003; Dobrovolskis et al., 2000; Alvarellos et al., 2002) and the dynamics of ejecta from Hyperion (Dobrovolskis and Lissauer, 2004). In this paper we test the specific hypothesis that Population II craters in the Saturn system are generated by ejecta from known impacts.

The paper is organized as follows. In Section 2 we briefly address the cratering process and cometary impact speeds. In Section 3 we discuss the choice of initial conditions and the choice of integrator for the ejected debris. In Sections 4–7 we address specific, large craters in the Saturn satellite system: Herschel on Mimas; Odysseus and Penelope on Tethys; and Tirawa on Rhea. These craters are fully described elsewhere (e.g., see Moore et al., 2004). We discuss the particles which survive the integrations in Section 8, while Section 9 summarizes our findings and states our conclusions. Finally Appendix A briefly describes our two ideal models for ejection of spalls or rubble.

2. Cratering and ejecta physics

Impact ejecta may be loosely divided between the near field (in which the details of the impact are important) and the far field (for which impact details are unimportant). The far field generally encompasses much the greater mass. The near field includes the highest energy densities and the highest ejection velocities; it includes jetting, and it includes the bouncing and chipping that occurs for the more oblique events. We will focus on the far field. Most ejecta are expelled during the main excavation flow stage of cratering (Chapman and McKinnon, 1986). The size and velocity of ejecta depend on both the impact speed and on the nature and composition of the target surface. The surfaces of the satellites of the outer planets are mostly composed of ices. Based on Galileo data, Bierhaus et al. (2001) provide evidence that most of the small craters (<2 km in diameter) on Europa are secondary craters. From this we infer that ejecta from icy satellites are capable of making sizeable craters.

2.1. Ejecta models

An ejection model useful for our purposes needs to predict the sizes and ejection velocities of the particles. If the impact occurs on a competent or hard surface, the ejecta resemble spalls. Melosh (1984, 1985a, 1989) developed a spallation theory in which a thin zone of competent target material close to the surface is subjected to relatively low pressures upon impact. The model predicts ejection of relatively large spall fragments at high velocities. Spallation is the accepted mechanism by which meteorites were ejected from the Moon and Mars. In addition, very large spalls are suspected of producing some of the large secondaries surrounding large impact basins such as Copernicus on the Moon and Lyot on Mars (Vickery, 1986, 1987). An unconsolidated regolith behaves differently. In such a case, the ejection speeds follow the model of Housen et al. (1983); their model does not provide estimates for ejecta sizes, but for that we again turn to Melosh (1984). We call this hybrid model the 'Rubble' model. We emphasize that these models are idealized in nature, and that real rock/ice fragmentation is probably much more complicated. In addition, we point out that Melosh's models provide *maximum* spall/ejecta sizes. We describe both ejection models in detail in Appendix A.

2.2. Crater size

After the main excavation flow is over, a bowl-shaped, transient crater is left at the target surface. Consider an impactor of diameter d km and density ρ_i striking the target surface of density ρ_t at a speed U km/s and at incident zenith angle ψ . Based on the work of Schmidt and Housen (1987), Zahnle et al. (2003) derive the following expression for the diameter of a simple/transient crater in km:

$$D_t = 1.1 \left(\frac{U^2}{g} \right)^{0.217} \left(\frac{\rho_i \cos \psi}{\rho_t} \right)^{0.333} d^{0.783}, \quad (1)$$

where g is the acceleration of gravity in km/s^2 at the target surface. For craters larger than a certain critical diameter D_c , the crater loses the simple bowl-shape and slumps into a wider, flatter dish-shaped crater. For Mimas, Tethys, and Rhea $D_c = 15$ km (Zahnle et al., 2003; but see also Moore et al., 2004); hence, for $D_t > 15$ km the final crater diameter D_f is approximated by

$$D_f = 0.7 D_t^{1.13} \quad (2)$$

(Zahnle et al., 2003). In contrast, $D_f = D_t$ for $D_t \leq 15$ km. Note that the equations for D_t and D_f are consistent with both the spallation and rubble models.

2.3. Heliocentric impact speed

Smith et al. (1981) provide a table of cometary impact speeds on Mimas, Tethys, Dione, and Rhea. Chapman and

Table 1

Crater data and impact speeds for ecliptic comets presumed to have produced craters Herschel, Odysseus, Penelope, and Tirawa. Latitude and longitude of Herschel, Odysseus, and Penelope are from [Batson \(1984\)](#). Latitude and longitude of Tirawa are from the USGS's Astrogeology Research Program website^a while the diameter of Tirawa is from Dr. P. Schenk's web site.^b β is the angular distance of the crater from the apex of motion in degrees, while $\langle U(\beta) \rangle$ is the expected impact speed of the ecliptic comet that made the given crater [Eq. (4)]. Estimated radii of the impactors are listed under the column labeled $d/2$ and were obtained using Eqs. (1) and (2)

Crater	Radius (km)	Lat (°)	Lon (°)	β (deg)	$\langle U(\beta) \rangle$ (km/s)	$d/2$ (km)
Herschel	65.0	0.0	104.0	14.3	30.9	2.3
Odysseus	200.0	30.0	130.0	48.4	23.1	12.5
Penelope	80.0	-10.0	252.0	159.5	10.2	7.0
Tirawa	187.5	34.2	151.7	66.9	16.4	16.0

^a <http://astrogeology.usgs.gov/Projects/SaturnSatellites>.

^b <http://www.lpi.usra.edu/research/outerp/rhea.html>.

[McKinnon \(1986\)](#) provide a table of impact speeds of heliocentric objects on various moons in the Solar System¹; this table is based on the work of [Shoemaker and Wolfe \(1982\)](#). [Horedt and Neukum \(1984\)](#) independently compute generally slightly higher impact speeds. Using Monte Carlo simulations based on [Levison and Duncan's \(1997\)](#) studies of the orbital dynamics of ecliptic comets, [Zahnle et al. \(2003\)](#) tabulate mean impact speeds for objects in the outer Solar System. In addition, they find that the mean normal component of the impact velocity, weighted by impact probability, is ([Zahnle et al., 2001](#))

$$\langle U_{\perp}(\beta) \rangle \approx v_{\text{orb}}(1 + 0.66 \cos \beta), \quad (3)$$

where β is the angular distance of the impact site from the apex of motion and v_{orb} is the satellite's circular orbital speed. The mean total impact speed, as obtained using [Zahnle et al.'s \(2001\)](#) Monte Carlo algorithm can be approximated by

$$\langle U(\beta) \rangle \approx \sqrt{3}v_{\text{orb}}(1 + 0.9 \cos \beta)^{0.35}. \quad (4)$$

The different dependencies on apex angle β seen in Eqs. (3) and (4) result from a systematic trend in incidence angle: impacts near the apex of motion tend to be more nearly normal while impacts near the antapex are generally more oblique. In [Table 1](#) we show properties for Herschel, Odysseus, Penelope, and Tirawa; we also use Eq. (4) along with Eqs. (1) and (2) to estimate the sizes of the comets responsible for these giant craters.

3. Initial conditions and the integration model

We use the SWIFT integrator package ([Levison and Duncan, 1994](#)) to evolve the orbits of the ejecta. SWIFT, which is based on work by [Wisdom and Holman \(1991\)](#), is able

¹ They report the following impact speeds on the Saturn system: 21.9 km/s (Mimas); 18.3 km/s (Tethys); 15.2 km/s (Rhea).

to integrate the orbits of the massless test particles as well as the massive bodies using a choice of integrators. For this study we use their Regularized, Mixed Variable Symplectic integrator (RMVS3); one of its advantages is the ability to use relatively large time-steps. Another advantage of the RMVS3 method is that it can handle very close approaches/collisions between a test particle and a massive body, which are of great interest for this study. SWIFT can remove a test particle from the integration if it collides with a massive body. One of us modified SWIFT to (a) detect collisions with Saturn's rings and (b) include high order oblateness terms for Saturn ([Dobrovolskis and Lissauer, 2004](#)). In our ejecta integrations we include the gravitational attractions of Saturn, Mimas, Enceladus, Tethys, Dione, Rhea, Titan, Hyperion, and Iapetus. In some integrations we also include Telesto and Calypso, the co-orbitals of Tethys. The initial state vectors and gravitational constants were kindly provided by R. Jacobson (personal communication) in the form of barycentric initial positions and velocities of the Saturn system for Julian Ephemeris Day 2444240.5 (2-Jan-1980), expressed in Mean Earth Equator and Equinox of J2000. The initial state vectors for Telesto and Calypso were provided for the same Epoch but in the B1950 system, so they were precessed to the J2000 system. In addition, we modified SWIFT to include the gravitational perturbations of the Sun by treating it as a massive, distant satellite of Saturn; we added the masses of Jupiter and the inner planets to that of the Sun. Initial conditions for the Sun and inner planets were obtained from the DE200 JPL analytical Ephemeris for the Epoch above. Finally a rotation and a translation were performed to align the fundamental plane to Saturn's equator and to set the origin to the center of Saturn for our SWIFT integrations. [Table 2](#) gives an overview of the Saturn satellite system used in our integrations. For the Tethys co-orbitals we assumed a density of $\rho = 0.9 \text{ g/cm}^3$, while their diameters are from [McGhee et al. \(2001\)](#).

One way to measure the accuracy of our integrations is to compare our results to known properties of the system. For example, it is known that Mimas and Tethys are in a 4:2 mean motion resonance; [Harper and Taylor \(1993\)](#) indicate that this produces a libration with a large amplitude and long period in the mean longitudes of both satellites. This libration argument can be written as

$$\theta_{13} = 2\lambda_1 - 4\lambda_3 + \Omega_1 + \Omega_3, \quad (5)$$

where λ indicates mean longitude and Ω is the longitude of the ascending node; the subscript 1 corresponds to Mimas, while the subscript 3 corresponds to Tethys. (When referring to specific moons we use the subscripts 1, 2, 3, 4, etc., for Mimas, Enceladus, Tethys, Dione, etc.; in addition, we use the subscript 'p' to refer to 'planet' (Saturn) and 'm' to refer to a generic moon/satellite of Saturn.) According to [Harper and Taylor \(1993\)](#), θ_{13} oscillates about zero with a predicted period of 72 years. We computed this libration argument from our numerical results. This quantity

Table 2

Satellite masses, radii and orbital elements; the values of GM_m and R_m are from R. Jacobson. Orbital elements are from Murray and Dermott (1999). The semi-major axes values are shown in kilometers as well as in Saturn radii (in parenthesis). For Saturn, we use $GM_p = 3.7931268 \times 10^7 \text{ km}^3/\text{s}^2$; $R_p = 60,330 \text{ km}$; $J_2 = 16297 \times 10^{-6}$; $J_4 = -910 \times 10^{-6}$; see Dobrovolskis and Lissauer (2004) for the terms J_6 , J_8 , J_{10} , and J_{12}

Satellite	GM_m (km^3/s^2)	R_m (km)	a_m (km)	e_m	i_m ($^\circ$)	P_m (days)
Mimas	2.5	197	185,520 (3.08)	0.0202	1.53	0.942
Enceladus	4.9	251	238,020 (3.95)	0.0045	0.02	1.370
Tethys	45.0	524	294,660 (4.88)	0	1.09	1.888
Calypso	8.3×10^{-4}	15	294,660 (4.88)	0	0	1.888
Teleso	4.4×10^{-4}	12	294,660 (4.88)	0	0	1.888
Dione	70.2	559	377,400 (6.26)	0.0022	0.02	2.737
Rhea	154.0	764	527,040 (8.74)	0.0010	0.35	4.518
Titan	8978.2	2775	1,221,850 (20.25)	0.0292	0.33	15.945
Hyperion	1.0	143	1,481,100 (24.55)	0.1042	0.43	21.277
Iapetus	106.0	718	3,561,300 (59.03)	0.0283	7.52	79.330

Table 3

Additional properties for Mimas, Tethys, and Rhea. Here we tabulate the satellite Hill radii R_H , the escape velocities v_{esc} , the factor $v_{\text{min}}/v_{\text{esc}}$ [Eq. (6)], the moons' orbital speed v_{orb} , the acceleration of gravity at the satellite's surface g and the half-width of each satellite's clearing-zone, a_{clear} [Eq. (8)]. For Mimas, Tethys, and Rhea, the transition crater diameter $D_c = 15 \text{ km}$ is assumed

Satellite	R_H (km)	v_{esc} (km/s)	$\frac{v_{\text{min}}}{v_{\text{esc}}}$	v_{orb} (km/s)	g (cm/s^2)	a_{clear} (km)
Mimas	521	0.159	0.82	14.3	6.4	5,546
Tethys	2165	0.414	0.88	11.3	16.3	7,486
Rhea	5832	0.635	0.94	8.5	26.3	20,706

varies sinusoidally with time with an amplitude of 93 degrees and period of 67 years, in reasonably good agreement with the analytical predictions. Dobrovolskis and Lissauer (2004) independently confirmed the validity of this model of the Saturn system by testing properties such as the 4:3 Titan–Hyperion resonance and the precession of Iapetus' orbit.

To compute the initial conditions for the ejecta we proceed as follows. We start with the latitude and longitude of the center of an impact basin. This point becomes the origin of a topocentric coordinate system (Bate et al., 1971) on which we construct twenty concentric “ejection-annuli”; the inner radius of the innermost ejection annulus is approximately given by the impactor radius $d/2$, while the outer radius of the outermost annulus is set to the distance from the impact site where the ejection speed drops below the escape speed of the satellite.² We then compute the radii of the twenty ejection annuli in such a way that all have the same area. The actual ejection ring radii correspond to the mass median of each annulus. Then, given each ejection radii we compute the ejecta velocities according to the spallation or rubble model (see Appendix A).

Because of third body effects, ejecta can escape at speeds less than the classical two-body escape speed $v_{\text{esc}} = \sqrt{2GM_m/R_m}$, where G is the gravitational constant, while M_m and R_m are the moon's mass and radius, respec-

tively. Placing the ejectum-satellite-Saturn trio in the context of the Circular Restricted Three-Body Problem (CR3BP), Alvarellos et al. (2002) found a simple approximate expression for the minimum speed v_{min} needed by a particle to escape the satellite. Assuming the ejection angle is 45 degrees,

$$\frac{v_{\text{min}}}{v_{\text{esc}}} = \sqrt{\frac{R_H^2 - R_H R_m}{R_H^2 - R_m^2/2}}, \quad (6)$$

where the Hill radius R_H is defined as

$$R_H = a_m \left[\frac{M_m}{3(M_m + M_p)} \right]^{1/3} \quad (7)$$

and a_m is the moon's semi-major axis while M_p is the mass of the central planet. The basic idea is that the ejectum escapes if it reaches the Hill radius. See Table 3 for the Hill radii and other additional properties of Mimas, Tethys, and Rhea.

4. Ejecta from Tirawa, on Rhea

Rhea has a heavily cratered surface approaching saturation, especially for craters smaller than 30 km (see Morrison et al., 1986; Lissauer et al., 1988). Rhea has at least two large impact basins, Izanagi and Tirawa (there exists some evidence for a third large impact basin on Rhea; see Moore et al., 2004). We selected Tirawa as the source crater for our numerical simulations. Tirawa is located on the leading side of Rhea (see Table 1). We assume densities $\rho_i = 0.6 \text{ g}/\text{cm}^3$ and $\rho_t = 0.9 \text{ g}/\text{cm}^3$. We estimate that the projectile that

² To simplify matters, we did not map the flat topocentric coordinate system to the spherical surface of the satellite (i.e., the topocentric coordinate system is a flat plane tangent to the spherical satellite and touching it at the center of the crater).

Table 4

Ejection circumstances for Tirawa (on Rhea) according to the two ejection models used in the text and described in Appendix A. The first column gives the ejection ring number. The second column gives the ejection ring's radius x for rubble, while the third column gives the ejection speed [Eq. (A.10)]; the fourth column gives the maximum size of an ejected boulder sitting on top of regolith l_r [Eq. (A.12)]. The fifth column gives the radius x of the ejection rings for the case of spalls, while the sixth column gives the ejection speed [Eq. (A.3)]; the seventh column gives the ejection zenith angle ζ for spalls [Eq. (A.9)], while the rest of the columns give the spall dimensions z_s , w , and $\langle L \rangle$ (the spall length l_s can be obtained from the relation $\langle L \rangle = (6z_s l_s w / \pi)^{1/3}$). The ejection zenith angle for the rubble model has been set to 45° . Inputs to the model are assumed to be for ice, and are follows (Melosh, 1984): $C_L = 4.4$ km/s; Poisson ratio $\nu = 0.365$; Tensile strength $\sigma_t = 0.017$ GPa; Crushing strength $\sigma_c = 0.1$ GPa

n	Rubble			Spalls					
	x (km)	v_e (km/s)	l_r (m)	x (km)	v_e (km/s)	ζ ($^\circ$)	z_s (m)	w (m)	$\langle L \rangle$ (m)
1	22.9	2.25	26	26.7	2.10	6.7	68	1260	760
2	25.9	1.82	34	30.7	1.78	7.7	77	1570	880
3	28.3	1.55	43	33.9	1.56	8.5	85	1870	1000
4	30.4	1.37	50	36.6	1.40	9.1	94	2150	1110
5	32.2	1.24	58	38.9	1.28	9.7	101	2420	1220
6	33.8	1.13	66	41.0	1.18	10.2	109	2690	1330
7	35.3	1.05	73	42.9	1.09	10.7	116	2960	1430
8	36.6	0.98	80	44.6	1.02	11.1	123	3220	1530
9	37.9	0.93	88	46.2	0.96	11.5	130	3470	1630
10	39.1	0.88	95	47.8	0.91	11.9	137	3730	1730
11	40.2	0.83	102	49.2	0.86	12.3	144	3980	1830
12	41.3	0.80	109	50.5	0.82	12.6	150	4230	1920
13	42.3	0.76	116	51.8	0.79	12.9	157	4480	2020
14	43.3	0.73	123	53.0	0.75	13.2	163	4720	2120
15	44.2	0.71	130	54.1	0.72	13.5	169	4970	2210
16	45.1	0.68	137	55.3	0.69	13.8	176	5210	2300
17	45.9	0.66	144	56.3	0.67	14.1	182	5450	2400
18	46.7	0.64	151	57.4	0.65	14.3	188	5690	2490
19	47.5	0.62	158	58.4	0.62	14.6	194	5930	2580
20	48.3	0.60	165	59.3	0.60	14.8	200	6170	2670

made the Tirawa impact basin was a 32 km comet striking at 16.4 km/s at an angle $\psi = 45^\circ$, i.e., the most probable incident angle (Gilbert, 1893; Shoemaker, 1962). The uncertainty on the comet size is $\pm 30\%$.

If the ice on the surface is as strengthless as unconsolidated regolith, then the rubble model of ejection should hold; in this model, ejecta velocities should decay as a power of distance from the impact site. But if the surface has some inherent strength, the physics of ejection should follow the spallation model. According to Smith et al. (1981), irregular outlines of many of Rhea's craters may be evidence of a layer of rubble for the upper crust, rather than a competent surface. In Table 4 we show results representative of the two ejection models. Note the spall thickness is roughly equivalent to the size predicted by the rubble model (please see Appendix A), but the other spall dimensions are much larger; as can be seen from Table 4, spalls have extreme aspect ratios.

In Fig. 1 we show the ejection speeds of ejecta from Tirawa as a function of distance from the impact site; we plot ejection speeds both for the spalls and for rubble models. On the curves for spall and rubble models we also show the actual ejection rings.

In Fig. 2 we plot the ejecta size as a function of ejection speed. In the case of spalls we show two curves: if the characteristic block size is given by the spall thickness z_s then the lower spall curve applies, while if the characteristic size

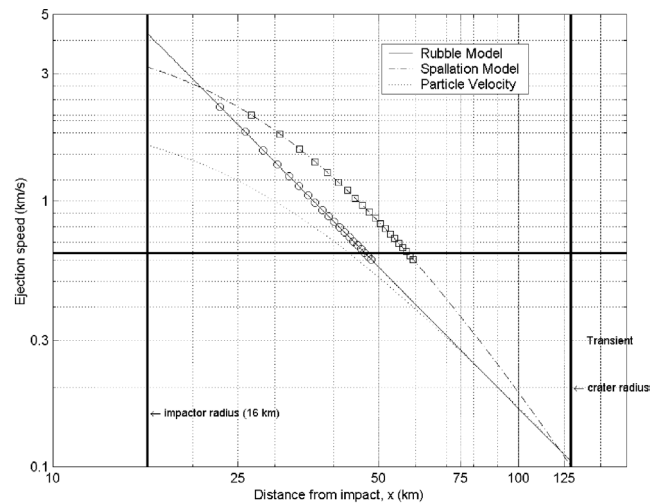


Fig. 1. Ejection speeds vs distance from impact for ejecta following the Tirawa impact event on Rhea. Two possible models are shown here. If the surface is competent then the spallation model of Melosh (1984) should apply; except for a region close to the impactor, this model gives the fastest ejection velocities [Eq. (A.3)]. On the contrary, if the surface is loose rubble, then the rubble model of Housen et al. (1983) should apply; this latter model follows a pure power law [Eq. (A.10)]. Ejection rings in our experiments are denoted by open circles (rubble) or squares (spalls) superimposed on the ejection velocity curves; hence, each circle/square represents 30 particles. The particle velocity given by Eq. (A.4) is also shown, as a dotted curve. The escape speed of Rhea (635 m/s) is shown as the horizontal line. The two thick vertical lines are the impactor radius (left) and the transient crater radius (right).

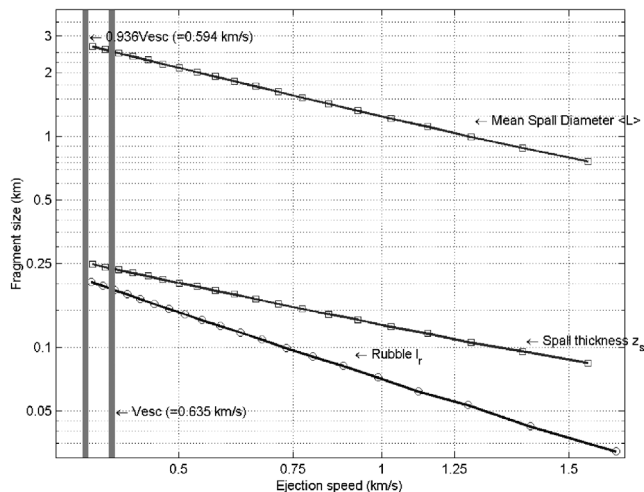


Fig. 2. Block sizes vs ejection speed v_e for the Tirawa formation event. The size of rubble ejecta as a function of ejection speed is given by Eq. (A.12) (lower curve). For spalls we give two sizes: the spall thickness z_s , given by Melosh’s (1984) Eq. (27) [for which Eq. (A.5) is an approximation] and the Mean Spall Diameter, $\langle L \rangle \equiv (6z_s l_s w / \pi)^{1/3}$, where l_s and w are the spall length and width, given by Eqs. (A.6) and (A.7), respectively. Ejection rings are denoted by open circles (rubble) or squares (spalls). No matter how we define the spall size, it is bigger than a ‘rubble’ particle. The left-most vertical line represents the minimum speed needed to escape Rhea $v_{\min} = 0.936v_{\text{esc}} \approx 597$ m/s [Eq. (6)], while the vertical line immediately to the right represents the escape speed of Rhea $v_{\text{esc}} \approx 635$ m/s.

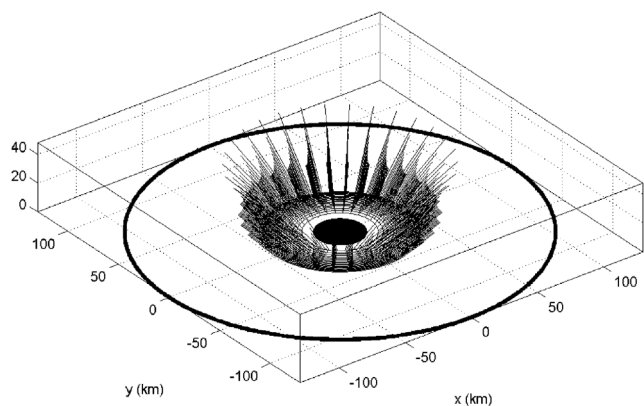


Fig. 3. Tirawa ejection circumstances for the rubble model (shown in a topocentric frame: x points South, y points East, and z points to the local vertical). For each of the twenty ejection rings we eject 30 test particles separated by 12 degrees in azimuth with initial speeds given by Eq. (A.10); the initial velocity vectors are all 45° . The ejection speeds of particles on the outermost ejection ring are approximately the minimum speed needed for escape, i.e., $0.936v_{\text{esc}} = 0.594$ km/s. The outermost thick ring represents the transient crater radius ($R_t \approx 130$ km). Ejection velocities beyond the outermost ejection ring are too low to escape Rhea and are not modeled in this paper. The filled black circle represents the size of the impactor ($d \approx 32$ km in diameter). The equivalent plot for the spallation model would look similar except that the velocity vectors would be more nearly vertical (see Table 4).

if given by the mean block diameter $\langle L \rangle$ (see Appendix A) the upper spall curve applies.

Fig. 3 illustrates the initial positions and velocity vectors predicted by the rubble model. Six hundred blocks were

ejected according to the rubble model and another six hundred were ejected according to the spallation model. These two sets were integrated independently using the RMVS3 algorithm of SWIFT for 15,000 years using the techniques presented in Section 3.

Of the 600 particles ejected using the rubble model, 18 did not escape, but went into suborbital paths. We filter out these cases by ignoring all ejecta that fall back in a time less than twice Rhea’s orbital period of 4.5 days. In a previous study (Alvarellos et al., 2002) we found that some Gilgamesh ejecta near the escape speed came back to Ganymede in a time comparable to the satellite’s orbital period, and yet these particles were neither on suborbital paths nor independent planetocentric orbits. Instead they were trapped into an intermediate orbital type, with fairly irregular and unstable orbits about the source satellite with a maximum distance of one Hill radius (Alvarellos et al., 2002, refer to these as “temporary, chaotic satellites”). Hence, our simple dividing criteria may not filter out these pathological orbits; however, in our previous study the number of objects in such orbits was quite small.

The 582 rubble particles that did escape spread out along the orbit of Rhea in just a few days. The evolution of the ejecta swarm is dominated by its interactions with Rhea. The result is a rapid clearing in Rhea’s neighborhood. Adjusting for the satellite’s eccentricity, Burns and Gladman (1998) give the half-width of the cleared zone as

$$a_{\text{clear}} \approx a_m e_m + 3.5 R_H, \quad (8)$$

where a_m and e_m are the moon’s semi-major axis and eccentricity, respectively. A particle with a semi-major axis within $\pm a_{\text{clear}}$ of a_m is expected to be removed due to either a collision with the satellite or a very close approach to it, which could fling the particle into a completely different orbit. An exception is particles trapped in 1:1 mean motion resonances, but we observed none. See Table 3 for the extent of the clearing zones of Mimas, Tethys, and Rhea.

Approximately 91% of the escapees eventually returned to Rhea; the rest of the particles had interesting fates (Table 5). Several hit Titan and Dione. There were two particles that made close flybys of Titan, which scattered them beyond one Saturn Hill radius (0.44 AU), at which point SWIFT removed them from the integration. Two particles were left orbiting Saturn at the end of this simulation. We will have more to say about these diehards later in this paper. See Table 5 for more details about the fate of Tirawa ejecta. All 600 particles ejected using the spallation model escaped Rhea; however, this set had somewhat less interesting fates than the previous case. Other than Rhea (which got 573 hits, or 95.5% of the total), only Dione and Titan were hit, with 4 particles surviving. We also ran an alternative set of simulations using cometary impact speeds from Chapman and McKinnon (1986); some other parameters such as the impactor and target densities are also different (see Table 5). The fates of ejecta for this alternative set of simulations are

Table 5

Fate of ejecta from crater Tirawa (on leading side of Rhea) after 15,000 years. There are two sets of results shown here. The leftmost set is the ‘nominal’ set discussed throughout the text while the rightmost set is an alternative set of results with initial conditions as indicated below.^a Although the initial conditions in the two sets are somewhat different, the results are qualitatively very similar. N is the number of particles. Percentages have been normalized to the number of particles that enter Saturn orbit. ‘Active’ means that the particles were still orbiting Saturn at the end of the integration. ‘Heliocentric’ means that the particle receded from Saturn a distance greater than one Saturn Hill radius (0.44 AU); particles that met these criteria were removed from the integration. Note that we obtained four hits on Saturn’s rings and three on Tethys in the alternative set of results

Target	Rubble		Spalls		Rubble ^a		Spalls ^a	
	N	Perc.	N	Perc.	N	Perc.	N	Perc.
Rings	0	0.0%	0	0.0%	4	0.7%	0	0.0%
Mimas	0	0.0%	0	0.0%	0	0.0%	0	0.0%
Enceladus	1	0.2%	0	0.0%	0	0.0%	0	0.0%
Tethys	0	0.0%	0	0.0%	3	0.5%	0	0.0%
Dione	27	4.6%	15	2.5%	24	4.1%	12	2.0%
Rhea	532	91.4%	573	95.5%	537	91.0%	572	95.3%
Titan	18	3.1%	8	1.3%	29	4.9%	14	2.3%
Hyperion	0	0.0%	0	0.0%	0	0.0%	0	0.0%
Heliocentric	2	0.3%	0	0.0%	3	0.5%	0	0.0%
Active	2	0.3%	4	0.7%	4	0.7%	2	0.3%
Escape	582	100%	600	100%	590	100%	600	100%

^a Alternative set of results. Initial conditions are different from the nominal results as follows: (a) Cometary impact speed $U \approx 15.2$ km/s (Chapman and McKinnon, 1986); (b) $\rho_i = 0.8$ g/cm³, $\rho_t = 1.0$ g/cm³; (c) Simple to complex crater transition from Zahnle et al. (1998); (d) $K \approx 0.5$; (e) Ten ejection rings; (f) We filtered out of the analyses those particles that returned in a time $t < 4.5$ days.

also listed in Table 5 for comparison; qualitatively this set of results is quite similar to the nominal set.

To investigate the extent of orbital dispersion of the impact ejecta, we provide estimates of their semi-major axes and eccentricities. It can be shown that the semi-major axis a of a particle launched from a satellite in a circular orbit with speed v_{orb} is to first order given by

$$a \approx a_m \left[1 + \frac{2\Delta v \cos \gamma}{v_{\text{orb}}} \right], \quad (9)$$

where γ is the angle between the apex of motion and the launch velocity vector $\Delta \mathbf{v}$. Its magnitude Δv is the hyperbolic excess speed of the ejectum, modified by third-body effects:

$$\Delta v = \sqrt{v_e^2 - v_{\text{min}}^2}, \quad (10)$$

where v_e is the speed of ejection and v_{min} is the minimum speed needed to escape, given by Eq. (6). The eccentricity of the ejectum is given by the simple formula

$$e \approx \frac{\sqrt{u^2 + 4w^2}}{v_{\text{orb}}} \quad (11)$$

(Weissman et al., 1989), where u and w are the radial and tangential components of $\Delta \mathbf{v}$, respectively. Note that $e \geq |a - a_m|/a_m$. The small additional velocity due to the satellite rotation is not taken into account in this simple analysis (although it is taken into account in the integrations).

We find that the apoapse distance of the fastest particles ejected from Tirawa using the rubble model is $Q = a(1 + e) \approx 8 \times 10^6$ km, almost enough to ‘dip’ into the inner boundary of Titan’s chaotic zone at 1.05×10^5 km (Duncan et al., 1989). Scattering by Rhea itself and third-body perturbations from Titan spread the orbits of these fastest ejecta,

thus enabling them to reach satellites in orbits adjacent to that of Rhea, and in one case, even Enceladus. Curiously, it seems that the main effect of Titan’s perturbations was to modify the orbits so that particles hit Dione more often than Titan itself. Faster ejection speeds would enable relatively more ejecta to reach Titan.

It is obvious from Table 5 that the vast majority of ejecta from Tirawa come back to Rhea; we wish to know where these particles hit, and we can obtain that information from SWIFT. At the time when SWIFT removes a particle, it creates a ‘snapshot’ of the state vectors of all the massive bodies plus the removed particle itself and saves this information to a file. We wrote a program which reads this file and computes the relative positions and velocities of the removed particle and Rhea. Then, using the Circular Restricted Three-Body Problem (CR3BP) as a model for the Saturn–Rhea–particle system, we integrate the particle until it impacts the surface of Rhea, at which point we record its impact location (Alvarillos et al., 2002). In Fig. 4a we plot the impact sites of the reaccreting ejecta. There is a clear tendency for Tirawa ejecta to hit the trailing side of Rhea more often than the leading side. Indeed, a combined histogram of impact longitudes (see Fig. 4b) shows an obvious minimum near the apex of motion. This behavior was also seen in the case of ejecta from crater Gilgamesh, located on the leading side Ganymede (Alvarillos et al., 2002), although in the latter case the leading vs trailing asymmetry was not as pronounced. During the Tirawa formation event, the ejecta are sprayed into individual planetocentric orbits which share at least three characteristics: (i) semi-major axes larger than that of Rhea, (ii) moderate eccentricities, and (iii) the orbits are tangent to Rhea’s. This means that on each periapse passage the particles have a good chance of encountering Rhea. During these encounters, the Tirawa ejecta overtake Rhea it-

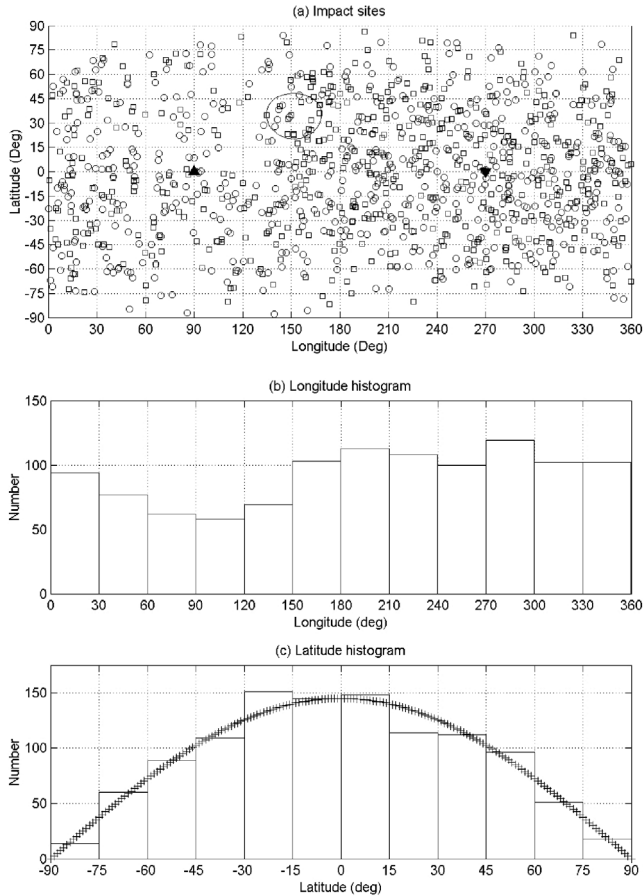


Fig. 4. (a) Impact sites of particles ejected from Tirawa that came back to Rhea after orbiting Saturn. The sub-Saturn point is located at the origin. The leading hemisphere runs from 0 to 180 degrees, while the trailing hemisphere runs from 180 to 360 degrees. Squares represent spalls, while circles represent rubble. The large oval represents the rim of Tirawa (375 km in diameter). The upward-pointing triangle represents the apex of motion, while the downward pointing triangle represents the antapex. Note that there seems to be a preference for the trailing side. Impact sites of particles on suborbital paths (18 from the rubble model) are not shown here. (b) Histogram of impact longitudes for ejecta from Tirawa accreting into Rhea. These particles were ejected from Tirawa (on Rhea’s leading side) using both the spallation and the rubble models. Note the minimum near the apex of motion (90°). (c) Histogram of impact latitudes; the heavy curve shows a plot of cosine of latitude.

self, and because it is in synchronous rotation the particles preferentially hit the trailing side.

Our program also gives us the impact velocities of the test particles upon accretion onto Rhea. From the particle identifier we can also know the size of the ejected particle (i.e., see Table 4). Hence, using Eq. (1) and setting $\rho_i = \rho_t$, we can compute the sizes of the poltorary craters these ejecta blocks would make upon impact. In Fig. 5 we show the impact speeds as a function of time. The mean impact speed increases with time, with typical speeds of about 1 km/s.

In a real impact, of course, the majority of ejecta would be suborbital and would either contribute to the ejecta blanket or (the larger blocks) generate classical secondaries. In addition, there will be a tail of countless small particles ejected

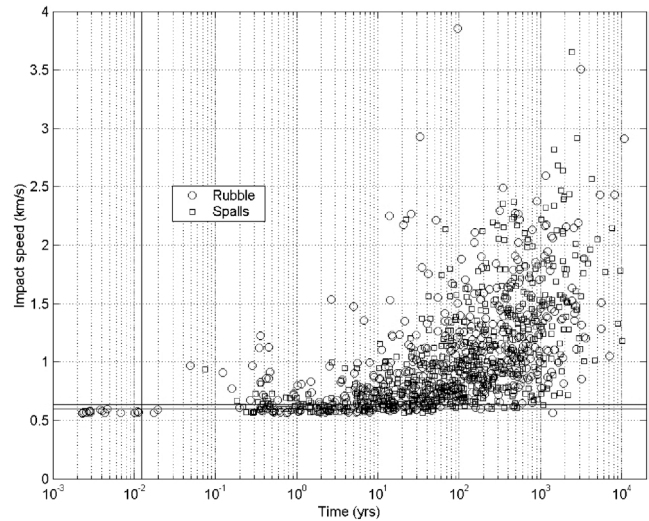


Fig. 5. Impact speeds vs time for ejecta from Tirawa accreting onto Rhea. The horizontal lines denote the escape speed of Rhea (v_{esc} and v_{min}) while the vertical line denotes the period of Rhea (4.52 days). The 18 rubble particles that went into suborbital trajectories are shown near or to the left of the vertical line. The mean impact speed increases with time. Typical impact speeds are ≈ 1.1 km/s, while the highest impact speeds are almost 4 km/s. The particles’ behavior tend to separate into roughly two groups. One small group clusters along the line indicating the escape speed of Rhea, but with removal/impact times less than twice the orbital period of Rhea; these are the suborbitals. The other, much more numerous group comes back to Rhea in times greater than the period of Rhea, and show a widening range of impact speeds with time, with the lower limit set by the escape speed of Rhea, and the upper limit showing a trend of increasing impact speeds with time; these are the particles that achieved saturnicentric orbits. Alvarellos et al. (2002) found similar divisions for ejecta from Ganymede.

with the same speeds, producing a ‘rain’ of small impacts in addition to the larger craters. However, here we have designed our study to focus on large ejecta that escape into planetocentric orbit. For example, using the scaling relationship of Housen et al. (1983) and Veverka et al. (1986), Moore et al. (2004) suggests that only between 15 and 20% of the material ejected during the formation of Tirawa would be able to escape Rhea.

For the rubble runs, a typical poltorary crater is about 1.0 km in diameter. In the case of spalls, the crater size depends on whether the ejecta size is characterized by the spall depth z_s or the mean block size $\langle L \rangle$. In the former case, we find a typical crater diameter is 1.4 km. If the latter, the craters on Rhea can be much larger, typically as big as 10 km across.

In Fig. 6 we plot the ejecta population as a function of time. It took approximately 90 and 150 years (rubble and spalls, respectively) for the population to decay to 50% of their original values. One can see from Fig. 6 that the population depletion does not behave like a simple exponential decay; for the span $10^1 < t < 10^3$ yr. the decay seems logarithmic.

The expected time-scale for accretion of particles on crossing orbits by a satellite is given by (Hamilton and

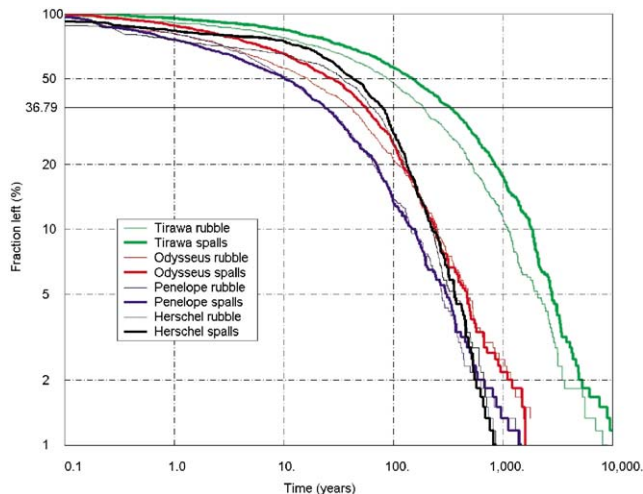


Fig. 6. Decay of particle populations ejected from large craters in the Saturn system as a function of time; note the log scales on both axes. The source crater is color coded (Tirawa: green; Odysseus: red; Penelope: blue; Herschel: black). The range of decay times is bracketed by the Penelope (fastest decay; time to remove 50% \approx 10 yr) and Tirawa spalls (slowest decay; time to remove 50% \approx 150 yr). The Herschel, Odysseus, and Penelope ejecta decay curves seem to cluster together, while the decay of ejecta from Tirawa stays apart from the other three.

Burns, 1994; Burns and Gladman, 1998)

$$T_{\text{coll}} \approx \pi \sqrt{\sin^2 i_m + \sin^2 \langle i_{\text{tp}} \rangle} \left(\frac{a_m}{R_m} \right)^2 \left(\frac{U_r}{U} \right) P_m. \quad (12)$$

Here i_m and i_{tp} are the inclination of the moon and test particle and a_m is the semi-major axis of the satellite. U is the speed of the test particle relative to the satellite, and U_r is the radial component of U ; Burns and Gladman (1998) state that for particles on crossing orbits U_r/U should be about 0.5. In our integrations, we find that the average inclination of a test particle at removal time is $\langle i_{\text{tp}} \rangle = 3.2$ degrees (average of rubble and spall runs); thus we estimate the sweep-up time for Rhea debris to be about $T_{\text{coll}} \approx 520$ years (about 24% of original ejecta left at this time). Note that T_{coll} is an estimate of the ‘e-folding’ time, which should be longer than the time needed to sweep up 50% of the population. None of the particles surviving at the end of the 15,000 year integrations (2 and 4 for the rubble and spall cases, respectively) had semi-major axes within the clearing zone of Rhea (Gladman, 1993; Burns and Gladman, 1998; see Table 3).

5. Ejecta from Odysseus, on Tethys

Tethys has a very large impact basin named Odysseus (200 km in radius) located in the leading hemisphere. Assuming that the impactor was traveling in a heliocentric orbit and that it struck Tethys at 23.1 km/s (see Table 1), we estimate using Eqs. (1) and (2) that its diameter was approximately 25 km.

We again model the ejection of debris from the crater in two different ways depending on the nature of the sur-

face of Tethys. The ejection circumstances for Odysseus are somewhat similar to Tirawa (Table 4), although the ejection speeds are slightly lower (10% less) and the ejecta block sizes are somewhat larger (about 25%) than for Tirawa. For example, the largest spall ejected from the Odysseus event is $\langle L \rangle \approx 3.6$ km. The largest spall ejected from Tirawa is $\langle L \rangle \approx 2.7$ km (see Table 4). The spall depth z_s , which may be a more realistic indication of the sizes of the ejecta blocks, is also slightly larger for Odysseus than for Tirawa. This is consistent with the smaller gravity on Tethys.

In addition to the classical satellites of Saturn, we also include in these simulations as massive bodies the two Tethys co-orbital companions Telesto (in the leading Lagrange point L_4) and Calypso (in the trailing Lagrange point L_5). The results of 2000 yr. integrations are summarized in Table 6. The dynamics of the ejecta swarm are dominated by interactions with Tethys itself, who cleans up most of its own debris. While the vast majority of particles were injected into higher orbits, we noted that Tethys scattered inward the closest members of the swarm. As these particles moved inward, their inclinations also increased from $i \sim 1$ degree to values in the range $2 < i < 7^\circ$. Between 8% and 16% hit Dione; a simple analysis using Eq. (9) shows that these ejecta were launched directly into Dione-crossing orbits. A few particles also hit Enceladus and Rhea (see Table 6).

Consider now Saturn, Tethys, and an ejectum: it is worth asking whether this ejectum can in principle reach the Lagrangian points where the co-orbitals are located. In the CR3BP, the Jacobi constant C is a conserved quantity³; see Szebehely (1967) for its definition. In this model, Tethys itself is assumed to travel around Saturn with zero eccentricity. It can be shown that for L_4 and L_5 , $C = 3.0$; an ejectum escaping from Tethys would need to have $C < 3.0$ in order to reach either Lagrange point. Given the initial conditions, it is relatively simple to compute each ejectum’s Jacobi constants: for the rubble integrations, 80% of the particles had $C < 3.0$, while for spalls, 85% had $C < 3.0$. In general, the most energetic particles come from the innermost ejection rings, and (unsurprisingly) these particles are the ones most likely to reach the L_4 or L_5 points. Although most of the Odysseus ejecta were in principle able to reach the co-orbitals, only one did (see Table 6). After 2000 years, there were seven rubble-particles and five spalls left in orbit about Saturn. None of these particles had semi-major axis values within Tethys’ clearing zone (see Table 3).

In Fig. 7 we show the orbital evolution of a sample spall. This specific particle was launched 54 km from the center of Odysseus at $v_e \approx 1.5v_{\text{esc}} = 0.61$ km/s at a zenith angle $\zeta = 17$ degrees (i.e., close to a vertical ejection), so that the particle easily escapes Tethys to achieve saturnicentric orbit. Since this particle was launched roughly in the direction of motion, it should achieve a semi-major axis of $a \approx 320,000$ km, while the eccentricity $e \approx 0.08$; these val-

³ The Tisserand parameter is an approximation to the Jacobi constant.

Table 6

Fate of ejecta from crater Odysseus (on leading side of Tethys) after 2000 years. There are two sets of results shown here. The leftmost set is the ‘nominal’ set discussed throughout the text while the rightmost set is a alternative set of results with initial conditions as indicated below.^a Although the initial conditions in the two sets are somewhat different, the results are qualitatively very similar. N is the number of particles. Percentages have been normalized to the number of particles that enter Saturn orbit. ‘Active’ means that the particles were still orbiting Saturn at the end of the integration. No particles hit either of Tethys’s co-orbitals in the nominal set of results, although one spall did hit Calypso in the alternative set

Target	Rubble		Spalls		Rubble ^a		Spalls ^a	
	N	Perc.	N	Perc.	N	Perc.	N	Perc.
Rings	0	0.0%	0	0.0%	0	0.0%	0	0.0%
Mimas	0	0.0%	0	0.0%	0	0.0%	0	0.0%
Enceladus	4	0.7%	2	0.3%	3	0.5%	3	0.5%
Tethys	496	89.4%	489	82.2%	497	88.4%	489	81.5%
Calypso	0	0.0%	0	0.0%	0	0.0%	1	0.2%
Telesto	0	0.0%	0	0.0%	0	0.0%	0	0.0%
Dione	45	8.1%	97	16.3%	54	9.6%	95	15.8%
Rhea	3	0.5%	2	0.3%	5	0.9%	12	2.0%
Titan	0	0.0%	0	0.0%	0	0.0%	0	0.0%
Hyperion	0	0.0%	0	0.0%	0	0.0%	0	0.0%
Heliocentric	0	0.0%	0	0.0%	0	0.0%	0	0.0%
Active	7	1.3%	5	0.8%	3	0.5%	0	0.0%
Escape	555	100%	595	100%	562	100%	600	100%

^a Alternative set of results. Initial conditions are different from the nominal results as follows: (a) Cometary impact speed $U \approx 18.3$ km/s (Chapman and McKinnon, 1986); (b) $\rho_i = 0.8$ g/cm³, $\rho_t = 1.0$ g/cm³; (c) Simple to complex crater transition from Zahnle et al. (1998); (d) $K \approx 0.5$; (e) Ten ejection rings; (f) We filtered out of the analyses those particles that returned in a time $t < 1.9$ days.

ues are consistent with what we see in Fig. 7 around $t = 0$; the periaapse distance from Saturn $q = a(1 - e)$ is approximately the same as the semi-major axis of Tethys itself a_3 . This particle makes close approaches to Tethys every periaapse passage. The longitude of the ascending node Ω (not shown) regresses almost uniformly over time with a period of 5.6 yr, while the argument of periaapse ω (not shown) advances with a period of 6.1 yr; this behavior is expected for a particle in a low inclination orbit around an oblate planet. Ultimately this particle hit Tethys at $t = 115$ years at longitude = 267 degrees and latitude = 0.4 degrees (see Fig. 8a) with an impact speed of 1.01 km/s. Depending on which spall size we use ($z_s \approx 150$ m or $\langle L \rangle \approx 2$ km) the resulting impact crater is approximately either 1.5 or 11.7 km across, respectively.

Like our sample particle, the majority of the ejecta came back to Tethys; in Fig. 8a we plot their impact sites. Again, we see that there is a tendency to hit the trailing side more often than the leading side and the reasons are the same as for Tirawa on Rhea. In Fig. 6 we plot the population decay for rubble and spalls. The decay curves are very similar to the decay curves of the ejecta from Tirawa, only in this case the time-scales are shorter; it took approximately 17 and 27 years (rubble and spalls, respectively) for the original populations to decay to half of their original values. The average inclination of the particles hitting Tethys is 2.0 degrees so that Eq. (12) gives the characteristic collision time $T_{\text{coll}} \approx 100$ years (23% of particles left at this time), again just within an order of magnitude of what we have recorded. Finally, in Fig. 9 we plot of the impact speeds of particles; again the average impact speed seems to increase as a function of time. Using Eq. (1), we find that for the rubble model a typical crater diameter is 1.2 km (maximum crater size is

2.8 km). For spalls, typical crater diameters come out to 1.5 or 10.2 km, depending on whether we use the spall depth z_s or the mean spall diameter $\langle L \rangle$ as the characteristic size. The biggest craters are 10.2 and 19 km in diameter, respectively.

6. Ejecta from Penelope on Tethys

Penelope is a large, 160 km crater located on the trailing side of Tethys. By running integrations of particles from Penelope, we can compare with the results obtained from Odysseus and directly see the effects of ejection from a leading vs a trailing side of a satellite. Using Eq. (4) we estimate that the object that made Penelope was traveling at 10.2 km/s and using Eqs. (1) and (2) we estimate its diameter as $d \approx 13.8$ km. Since this comet was smaller and slower than the one that made Odysseus, the spallation and rubble models predict generally smaller and slower ejecta blocks. The integrations of ejecta from Penelope also included Telesto and Calypso and ran for 2000 years, as for the Odysseus ejecta simulation; approximately 79% of the ejecta are able to reach the co-orbitals (i.e., $C < 3.0$). Table 7 summarizes the results.

Comparing Table 7 to Table 6 for Odysseus ejecta, we see that as expected, Penelope ejecta have a greater tendency to hit satellites interior to Tethys, because the particles are injected into moderately eccentric orbits with semi-major axes *smaller* than that of Tethys itself. That relatively more ejecta came back to Tethys in this case than in the Odysseus case can be mostly attributed to the higher velocity of the Odysseus impactor: 23 vs 10 km/s. Hence the particles from Odysseus are ejected faster than particles from Penelope and have a greater chance of interactions/impacts with other

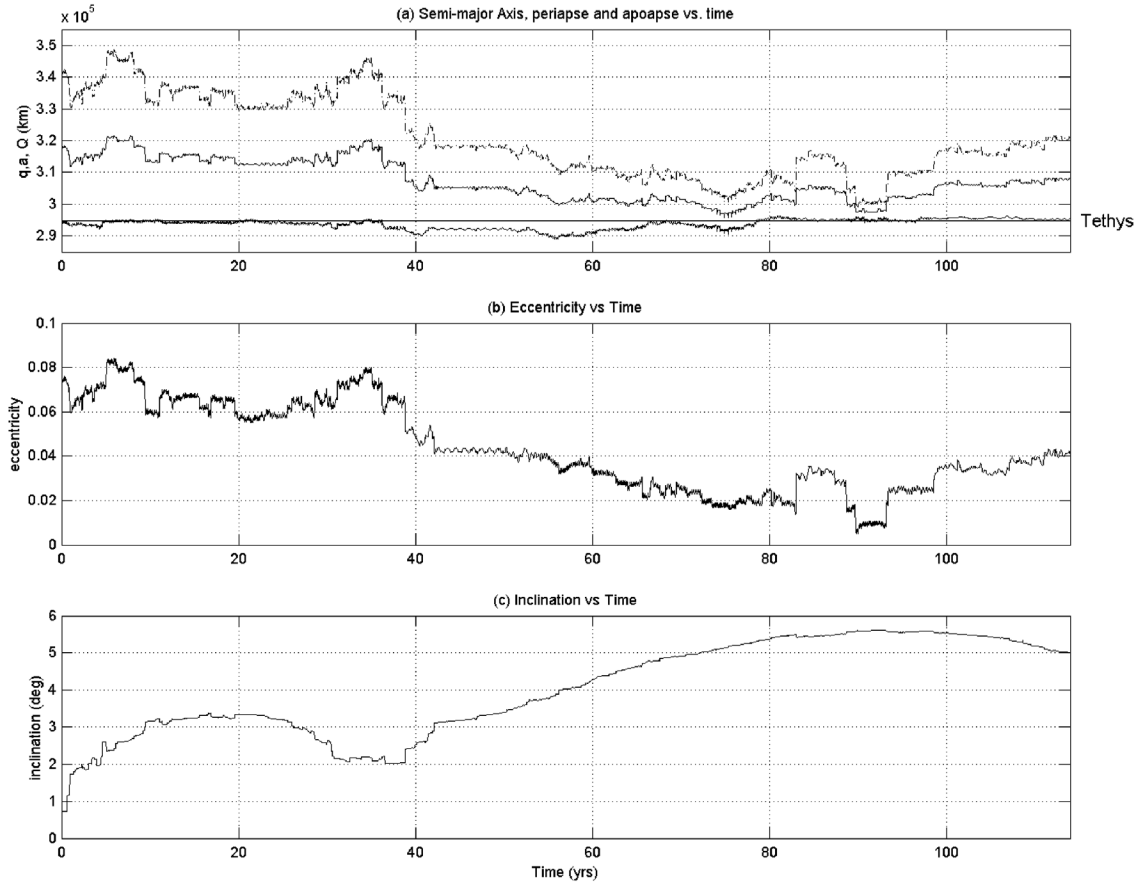


Fig. 7. Orbital evolution of a spall ejected from Tethys. Particle was launched from $x = 54$ km from the center of Odysseus at $v_e = 0.61$ km/s at a zenith angle $\zeta = 17^\circ$. (a) Semi-major axis a , periapse distance q and apoapse distance Q vs time; (b) Eccentricity e ; (c) Inclination i (measured from Saturn's equatorial plane) vs time. Each close approach to Tethys is like an impulsive ' Δv ' acting on the ejectum's orbit: when $q < a_3$ (Tethys' semi-major axis), as for the span $35 < t < 68$ yr, the Δv is negative (i.e., Tethys' gravity slows down the particle) and lowers the apoapse distance Q ; conversely when $q > a_3$ the Δv is positive. Note that through the whole ordeal q varies slightly, but on average $q \approx a_3$ as expected. At the same time, the eccentricity e generally decreases, while the inclination i increases. The particle finally hit Tethys 115 years after launch at (long., lat.) = $(267^\circ, 0.4^\circ)$, very near the antapex.

Table 7

Fate of ejecta from crater Penelope (on trailing side of Tethys) after 2000 years. There are two sets of results shown here. The leftmost set is the 'nominal' set discussed throughout the text while the rightmost set is an alternative set of results with initial conditions as indicated below.^a Although the initial conditions in the two sets are somewhat different, the results are qualitatively very similar. N is the number of particles. Percentages have been normalized to the number of particles that enter Saturn orbit. 'Active' means that the particles were still orbiting Saturn at the end of the integration. One spall hit co-orbital Telesto in the nominal set and one spall hit Calypso in the alternative set

Target	Rubble		Spalls		Rubble ^a		Spalls ^a	
	N	Perc.	N	Perc.	N	Perc.	N	Perc.
Rings	0	0.0%	0	0.0%	0	0.0%	0	0.0%
Mimas	0	0.0%	0	0.0%	5	0.9%	5	0.8%
Enceladus	16	2.9%	34	5.8%	25	4.4%	38	6.4%
Tethys	538	95.9%	548	92.9%	526	93.4%	541	91.7%
Calypso	0	0.0%	0	0.0%	0	0.0%	1	0.2%
Telesto	0	0.0%	1	0.2%	0	0.0%	0	0.0%
Dione	4	0.7%	3	0.5%	4	0.7%	5	0.8%
Rhea	0	0.0%	0	0.0%	0	0.0%	0	0.0%
Titan	0	0.0%	0	0.0%	0	0.0%	0	0.0%
Hyperion	0	0.0%	0	0.0%	0	0.0%	0	0.0%
Active	3	0.5%	4	0.7%	3	0.5%	0	0.0%
Escape	561	100%	590	100%	563	100%	590	100%

^a Alternative set of results. Initial conditions are different from the nominal results as follows: (a) Cometary impact speed $U \approx 18.3$ km/s (Chapman and McKinnon, 1986); (b) $\rho_i = 0.8$ g/cm³, $\rho_t = 1.0$ g/cm³; (c) Simple to complex crater transition from Zahnle et al. (1998); (d) $K \approx 0.5$; (e) Ten ejection rings; (f) We filtered out of the analyses those particles that returned in a time $t < 1.9$ days.

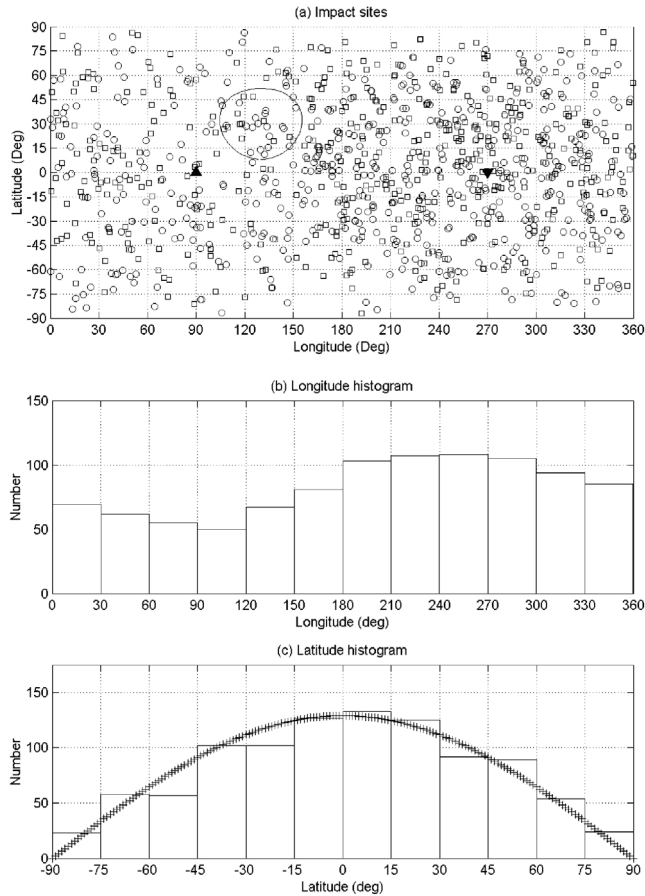


Fig. 8. (a) Impact sites of particles ejected from Odysseus that came back to Tethys after orbiting Saturn. The sub-Saturn point is located at the origin. The leading hemisphere runs from 0 to 180 degrees, while the trailing hemisphere runs from 180 to 360 degrees. Squares represent spalls, while circles represent rubble. The large, oval outline represents the rim of Odysseus (400 km in diameter). The upward-pointing triangle at 90 degrees represents the apex of motion, while the downward pointing triangle at 180 degrees represents the antapex. Note that there seems to be a slight preference for the trailing side. Impact sites of particles on suborbital paths (5 spalls and 45 rubble particles) are not shown here. (b) Histogram of impact longitudes for ejecta from Odysseus accreting into Tethys. These particles were ejected from Odysseus (on Tethys’s leading side) using both the spallation and the rubble models. Note the minimum near the apex of motion (90 degrees). (c) Histogram of impact latitudes; the heavy curve shows a plot of cosine of latitude.

satellites. Only one spall hit a co-orbital (Telesto); this was not merely a fluke, because we had also observed one spall from Penelope hitting the other co-orbital (Calypso) in our alternative simulations (see Table 7).

Fig. 6 plots the population of ejecta from Penelope as a function of time. The population decay of both swarms (rubble and spalls) is fairly similar. The times to remove 50% of material averages just 10 years (rubble and spalls). We note that ejecta from Penelope decay at a slightly faster rate than ejecta from Odysseus, consistent with their smaller orbits. At the end of the integration, there were still 3 rubble and 4 spall ejecta left, none of which remained within Tethys’ clearing zone (see Table 3). Since the average inclination of particles accreting into Tethys is 1.8 degrees, Eq. (12) predicts a col-

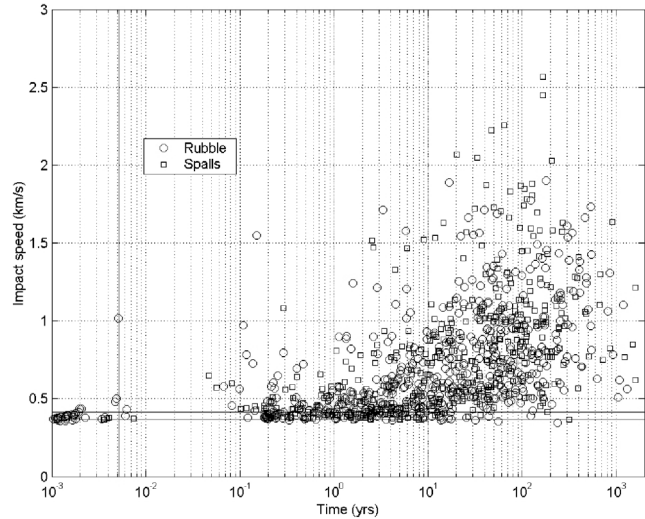


Fig. 9. Impact speeds vs time for ejecta from Odysseus accreting into Tethys. The horizontal lines denote the escape speed of Tethys as well as v_{\min} , while the vertical line denotes the period of Tethys (1.888 days). The mean impact speed increases with time. Note that the maximum spall impact speeds (≈ 2.6 km/s) are significantly higher than the maximum rubble impact speeds (≈ 1.9 km/s).

lision time-scale of $T_{\text{coll}} \approx 94$ years, at which point we only have 15% of the original population left.

In Fig. 10a we plot the impact sites of the particles on Tethys. In contrast to Odysseus (Fig. 8), Penelope ejecta preferentially hit the leading side of Tethys: this is essentially the mirror image of Odysseus. Penelope ejecta are near apoapse when encountering Tethys; hence Tethys overtakes them, and is therefore hit mostly on its leading face.

Fig. 11 shows impact speeds for particles from Penelope that got swept up by Tethys. The impact speeds are generally lower than for the Odysseus case (compare with Fig. 9); all impact speeds are below 1.8 km/s. Hence, the resulting craters are generally smaller than in the Odysseus case. In the case of spalls, a typical crater diameter is about 1.0 km, with a maximum of 1.7 km if we use the spall depth z_s as the characteristic size of the ejecta blocks. On the other hand, if we use the average spall length $\langle L \rangle$ as a characteristic ejecta size, then a typical crater size is about 6.1 km with a maximum crater diameter of 10.7 km. The rubble model (which uses l_r) predicts almost identical results to the spall model with z_s .

We can now do some (albeit limited) statistics in regards to impacts on the co-orbitals of Tethys. We ejected 1200 particles each from Odysseus and Penelope in the nominal run; we also ejected the same number of particles from each crater in the alternative run (see Tables 6 and 7) for a total of 4800 particles ejected from Tethys. Using the CR3BP as a model, roughly 81% of these were in principle able to reach the co-orbitals. Only three particles hit either Calypso or Telesto, meaning that $\sim 0.1\%$ of ejecta from Tethys were able to reach either co-orbital.

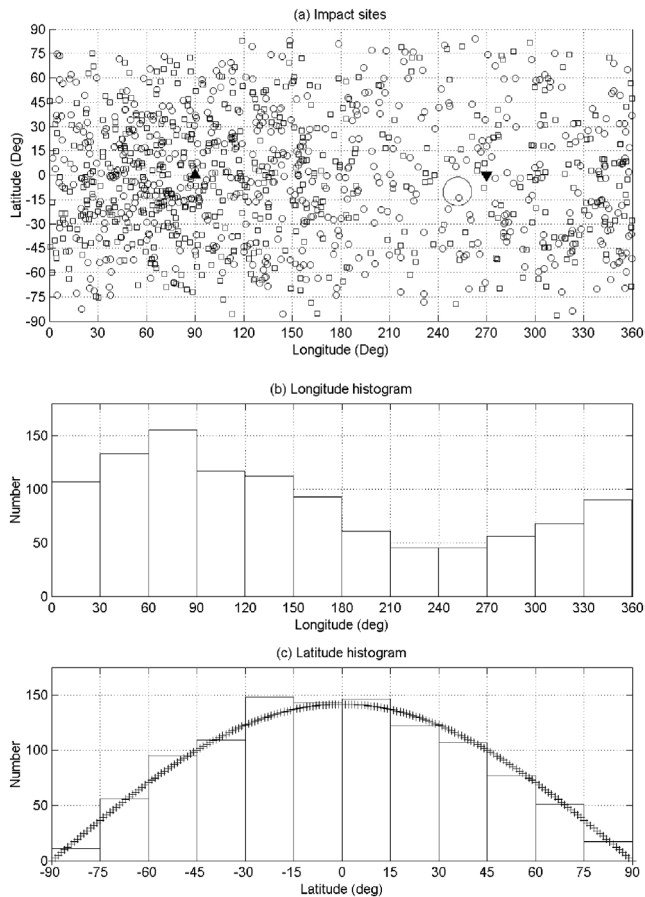


Fig. 10. (a) Impact sites of particles ejected from Penelope that came back to Tethys after orbiting Saturn. The sub-Saturn point is located at the origin. The leading hemisphere runs from 0 to 180 degrees, while the trailing hemisphere runs from 180 to 360 degrees. Squares represent spalls, while circles represent rubble. The large, oval outline represents the rim of Penelope (160 km in diameter). The upward-pointing triangle represents the apex of motion, while the downward-pointing triangle represents the antapex. Note that there seems to be a preference for the leading side. Impact sites of particles on suborbital paths (10 spalls and 39 rubble particles) are not shown here. (b) Histogram of impact longitudes for ejecta from Penelope accreting into Tethys. These particles were ejected from Penelope (on Tethys's trailing side) using both the spallation and the rubble models. Note the minimum near the antapex of motion (180 degrees). (c) Histogram of impact latitudes; the heavy curve shows a plot of cosine of latitude. Compare to Fig. 8.

7. Ejecta from Herschel, on Mimas

By far the most prominent surface feature on Mimas is Herschel, a large impact basin (1/3 of the diameter of Mimas) more or less centered on the leading hemisphere. Mimas is covered with small craters which seem to be uniformly distributed; other than Herschel, there are few craters larger than 50 km (Smith et al., 1981; Morrison et al., 1986). A plausible way to make Herschel is to have a 4.6 km diameter comet striking Mimas at 32 km/s. As before, six hundred particles are ejected using the rubble model and six hundred using the spallation model, and both sets are independently integrated for 1000 years.

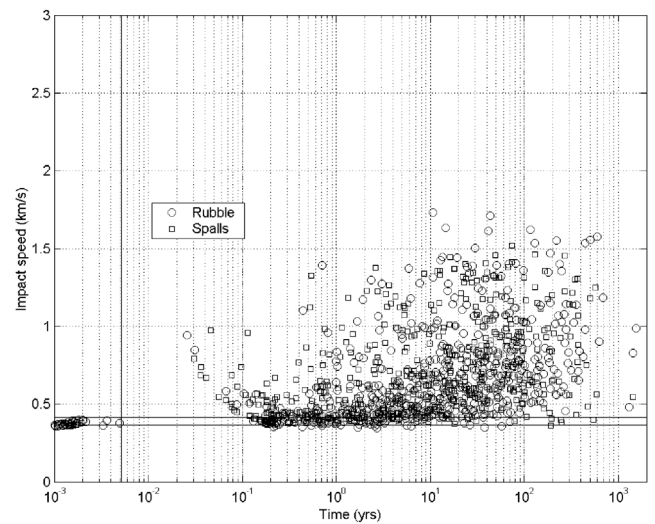


Fig. 11. Impact speeds vs time for ejecta from Penelope accreting into Tethys. The horizontal lines denote the escape speed of Tethys as well as v_{\min} , while the vertical line denotes the period of Tethys (1.888 days). The mean impact speed increases with time. Compare to Fig. 9; note that the average speeds are lower than in the Odysseus case.

The escaped particles spread out along the orbit of Mimas in just a few orbital periods. Decay curves are shown in Fig. 6. The time to sweep up 50% of material is $t_{1/2} \approx 39$ years. This is similar to what Burns and Gladman (1998) obtained numerically for ejecta from Mimas. In that study, they surrounded Mimas with a spherical cloud of particles moving radially away at 100 Mimas radii, which is far outside Mimas' Hill sphere. Note that their ejection circumstances are very different and yet the half-life in their numerical experiment is similar to ours. In our numerical experiments, the average inclinations of particles swept up by Mimas is 1.7 degrees, so that Eq. (12) predicts $T_{\text{coll}} \approx 140$ years (at which time we are left with only 18% of the original population). As can be seen in Table 8, almost all Herschel ejecta eventually reaccrete on Mimas, as predicted by Smith et al. (1981). Due to its small mass, Mimas is not very efficient at scattering its own debris; however, several spalls (4%) did reach Enceladus, probably because spalls are ejected slightly faster than the particles ejected with the rubble model. Fig. 12a shows the impact sites of Herschel ejecta. As expected, more ejecta hit the trailing side of Mimas, opposite Herschel, but the cratering asymmetry is especially pronounced here (see Fig. 12b). In Fig. 13 we plot the impact speeds of ejecta with Mimas. The average impact speed tends to increase with time, but typical speeds are less than 1 km/s. For rubble, expected crater sizes come to ~ 1 km in diameter, while for spalls the typical crater diameters come to about 0.9 km and 6.3 km. After the 1000 year integration we find three spalls and two rubble ejecta still orbiting Saturn. One of the rubble particles is still in a Mimas-crossing orbit. The other four survivors have reached interesting orbits, as considered in the next section.

In Fig. 14 we show snapshots of the positions of the particles at four different times in the 1000 year simulation. The

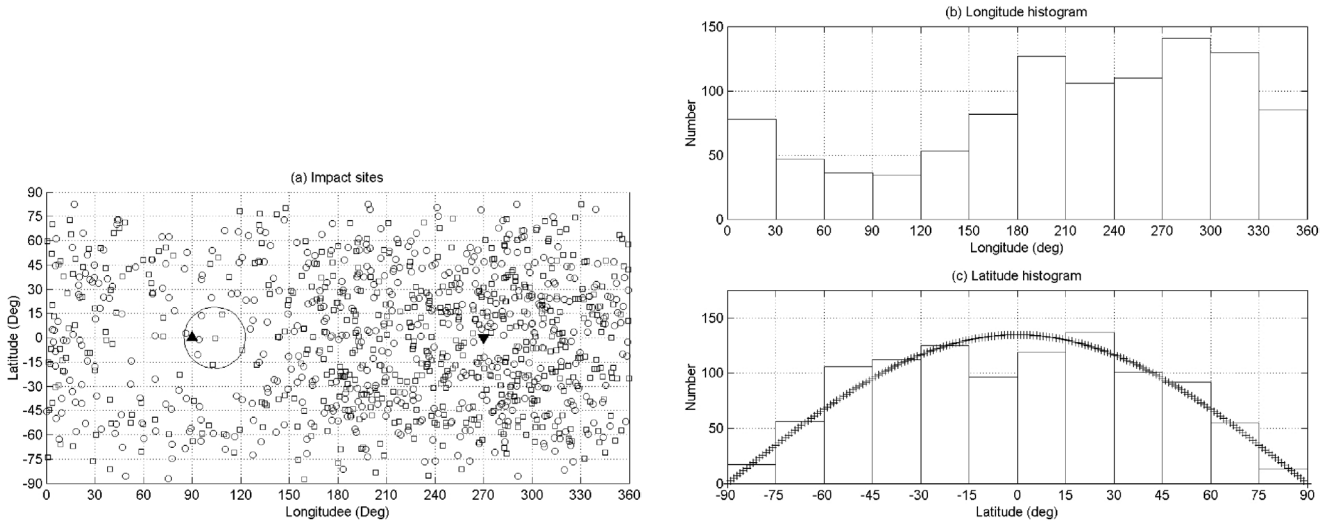


Fig. 12. Impact sites of particles ejected from Herschel that came back to Mimas after orbiting Saturn. The sub-Saturn point is located at the origin. The leading hemisphere runs from 0 to 180 degrees, while the trailing hemisphere runs from 180 to 360 degrees. Squares represent spalls, while circles represent rubble. The large, oval outline represents the rim of Herschel (130 km in diameter). The upward-pointing triangle represents the apex of motion, while the downward-pointing triangle represents the antapex. Note that there seems to be a strong preference for the trailing side. Impact sites of particles on suborbital paths (46 spalls and 74 rubble particles) are not shown here. (b) Histogram of impact longitudes for ejecta from Herschel accreting into Mimas. These particles were ejected from Herschel (on Mimas' leading side) using both the spallation and the rubble models. Note the minimum near the apex of motion (90 degrees). (c) Histogram of impact latitudes; the heavy curve shows a plot of cosine of latitude; note the curious minimum over the equatorial regions.

Table 8

Fate of ejecta from crater Herschel (on leading side of Mimas) after 1000 years. There are two sets of results shown here. The leftmost set is the 'nominal' set discussed throughout the text while the rightmost set is an alternative set of results with initial conditions as indicated below.^a Although the initial conditions in the two sets are somewhat different, the results are qualitatively very similar. N is the number of particles. Percentages have been normalized to the number of particles that enter Saturn orbit. 'Active' means that the particles were still orbiting Saturn at the end of the integration. Most ejecta returned to Mimas

Target	Rubble		Spalls		Rubble ^a		Spalls ^a	
	N	Perc.	N	Perc.	N	Perc.	N	Perc.
Rings	0	0.0%	0	0.0%	0	0.0%	0	0.0%
Mimas	524	99.6%	529	95.5%	530	99.3%	527	93.4%
Enceladus	0	0.0%	22	4.0%	0	0.0%	32	5.7%
Tethys	0	0.0%	0	0.0%	0	0.0%	0	0.0%
Dione	0	0.0%	0	0.0%	0	0.0%	0	0.0%
Rhea	0	0.0%	0	0.0%	0	0.0%	0	0.0%
Titan	0	0.0%	0	0.0%	0	0.0%	0	0.0%
Hyperion	0	0.0%	0	0.0%	0	0.0%	0	0.0%
Heliocentric	0	0.0%	0	0.0%	0	0.0%	0	0.0%
Active	2	0.4%	3	0.5%	4	0.7%	5	0.9%
Escape	526	100%	554	100%	534	100%	564	100%

^a Alternative set of results. Initial conditions are different from the nominal results as follows: (a) Cometary impact speed $U \approx 21.9$ km/s (Chapman and McKinnon, 1986); (b) $\rho_i = 0.8$ g/cm³, $\rho_t = 1.0$ g/cm³; (c) Simple to complex crater transition from Zahnle et al. (1998); (d) $K \approx 0.5$; (e) Ten ejection rings; (f) We filtered out of the analyses those particles that returned in a time $t < 0.9$ days.

particles mostly stay in the general vicinity of Mimas, which gradually depletes the swarm population.

8. A note on survivors

In these simulations the vast majority of ejecta are accreted by one satellite or another; most end up back on the moon from which they came, since ejecta start on orbits that perforce intersect the source satellite's orbit (Burns and Gladman, 1998). There were a few particles left in orbit

around Saturn at the end of some integrations. The issue we now explore is whether some of these survivors display signs of long-term stability or other interesting characteristics. In Fig. 15 we plot orbital characteristics of these survivors. Most tend to remain in orbits similar to that of the source satellite, but there were two particles ejected from Tirawa that managed to achieve high inclination, high eccentricity orbits via interactions with Titan. In Fig. 16 we see a plot of the orbital elements as a function of time for one of these survivors, a rubble particle ejected from Tirawa (shown as the particle with $i \approx 20$ degrees and $a \approx 4.4 \times 10^6$ km in

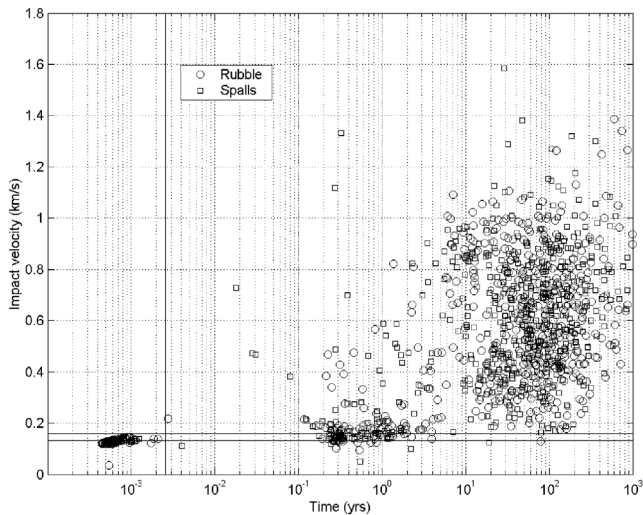


Fig. 13. Impact speeds vs time for ejecta from Herschel accreting into Mimas. The horizontal lines denote the escape speed of Mimas as well as v_{\min} , while the vertical line denotes the period of Mimas (0.942 days). The mean impact speed increases with time.

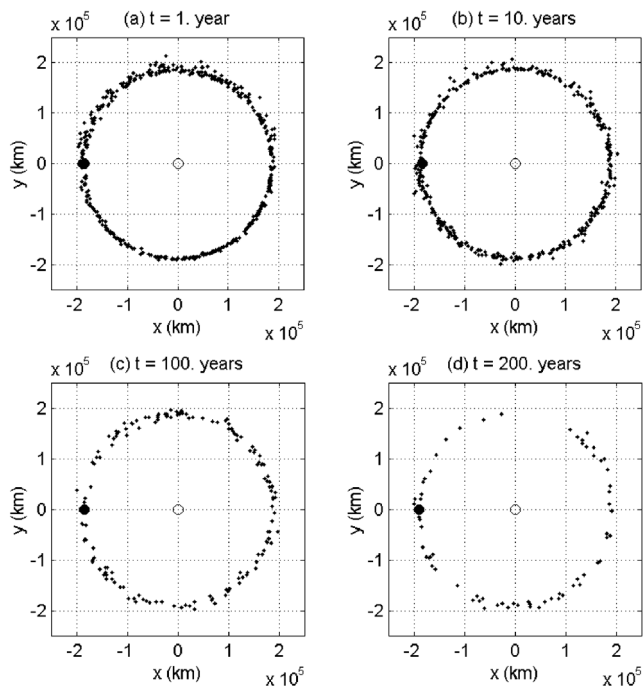


Fig. 14. Snapshots of position at four different times for the Mimas rubble simulation. The positions have been rotated by an angle such that Mimas is located on the neg. x -axis while Saturn lies at the origin. (a) $t = 1$ year, fraction of original pop. left = 91%; (b) $t = 10$ years, fraction of original pop. left = 78%; (c) $t = 100$ years, fraction of original pop. left = 48%; (d) $t = 200$ years, fraction of original pop. left = 35%. The particles generally do not get scattered very widely and stay in the general vicinity of Mimas, who proceeds to accrete its own debris.

Fig. 15). This particle underwent a close approach to Titan around $t \approx 300$ yr, which resulted in a quick and dramatic increase of its semi-major axis, eccentricity and inclination. For $t > 300$ years the particle is in a Iapetus-crossing orbit and goes into and out of resonances with Titan; strong

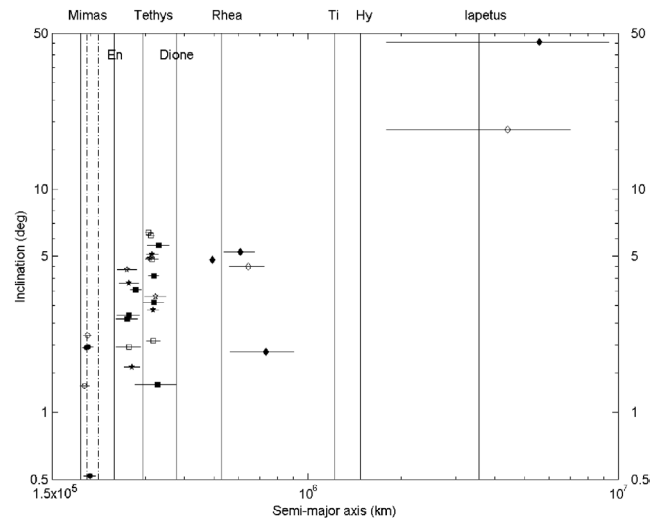


Fig. 15. Inclinations vs distances for the survivors at the end of the integrations. The error bars are centered on the semi-major axis a (the ‘mean’ distance from Saturn) of the surviving particle, while the minimum and maximum distances for a particle are the quantities $q = a - ae$ and $Q = a + ae$, respectively and are shown as the upper and lower limits of the error bars; hence, the plot gives an idea of the a , e , i distribution of the survivor particles. Spall survivors are filled in. The semi-major axes of Saturn’s major satellites are shown as vertical lines. We use dashed lines for the recently discovered moonlets orbiting between Mimas and Enceladus: ‘Methone’ (left) and ‘Pallene’ (right). The symbols indicate the source crater of the surviving particles as follows. Diamonds: Tirawa (lasted 15,000 yr); Squares: Odysseus (lasted 2000 yr); Stars: Penelope (lasted 2000 yr); Circles: Herschel (lasted 1000 yr). Note that most survivors are located in low inclination, low eccentricity orbits. The exception are two particles ejected from Tirawa; these two particles were scattered to Iapetus-crossing orbits by close encounters with Titan. For comparison, distant, irregular Phoebe is outside of the plot at $a \approx 13 \times 10^6$ km. All the survivors from Tethys stay relatively close to Tethys itself: those ejected from Odysseus (Penelope) generally went to higher (lower) orbits. The survivors ejected from Herschel stay in orbits slightly higher than that of Mimas; one of these was left in a Mimas-crossing orbit. The others are left in orbits similar ($a \approx 194,000$ km) to that of the recently discovered moonlet S/2004 S1 (‘Methone’).

solar perturbations play a role in the evolution of its orbital elements as well. Interestingly, further extending the integrations out to 30,750 years showed that this particle is stable over such time-scales. The other survivors from Tirawa went into moderately eccentric orbits slightly higher than Rhea’s, except for one left in an almost circular orbit with $i \sim 5^\circ$.

Tethys survivors (Fig. 15) were left on local orbits; one Odysseus ejectum was left in a Tethys-crossing orbit, meaning that its near-term fate is most likely a collision. The eccentricities and inclinations are generally low (< 6 degrees). Survivors from Odysseus settled on orbits with semi-major axes slightly larger than that of Tethys, while survivors from Penelope were left on orbits with smaller semi-major axes than Tethys’, as expected from Eq. (9).

Finally we examine the five ejecta from Herschel which were still orbiting Saturn 1000 years after ejection from Mimas (see Fig. 15); these tend to be of the smaller, faster variety. One of these (rubble) is still in a Mimas-crossing orbit, so its near term fate is probably a direct hit on its

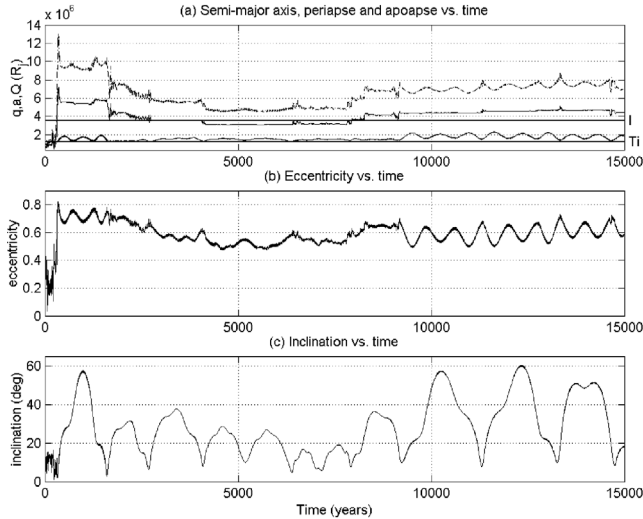


Fig. 16. Evolution of the orbital elements of a rubble particle ejected from Tirawa; a close approach to Titan at $t \approx 300$ yr raised its semi-major axis, eccentricity and inclination, a process that left it in a Iapetus-crossing orbit. This particle survived the 15,000 year integration and it is also shown in Fig. 15. (a) Semi-major axis a , periape distance q and apoapse distance Q as a function of time. It undergoes at least two mean-motion resonances with Titan, namely a 1:5 ($2800 < t < 4000$ yr; also a near 1:1 mean-motion resonance with Iapetus) and a 1:4 ($4200 < t < 6400$ yr). Up until $t \approx 9200$ years, this particle could have made further close approaches to Titan at periape passage, when its q oscillated about $\approx 1.45 \times 10^7$ km; after that its mean value increased to $\approx 1.8 \times 10^7$ km. The approximate semi-major axes of Titan and Iapetus are marked to the right of the plot as ‘Ti’ and ‘I’, respectively. (b) Eccentricity vs time. Its maximum value is $e \approx 0.8$ soon after the close approach to Titan, then it slowly decreases to $e \approx 0.5$ until $t \approx 9000$ year, after which the eccentricity oscillates semi-regularly about $e \approx 0.6$. (c) Inclination i (measured with respect to Saturn’s equator) as a function of time. Soon after the close approach to Titan the inclination increases dramatically to a maximum value of $i \approx 60^\circ$, but it quickly decreases soon after. As can be seen, this behavior is quasi-periodic (with a period of ≈ 1300 years) as this orbit precesses from near Saturn’s equatorial plane to the opposite side of Saturn’s orbital plane under strong solar gravitational perturbations. This particle is stable for at least $\sim 30,000$ years.

source satellite (indeed further integrations showed it hit Mimas soon after around $t = 1300$ yr). The other four particles all have similar orbits in that their semi-major axes (ranging from 193,000 to 199,000 km) are slightly higher than Mimas’, and have low eccentricities (< 0.04) and relatively low inclinations (< 2.2 degrees). These orbits somewhat resemble that of S/2004 S1 (‘Methone’), one of the moonlets recently discovered by Cassini between Mimas and Enceladus (IAU Circular 8389); its semi-major axis, eccentricity and inclination are reported to be 194,251 km; $e = 0.001$; $i = 0.018$ degrees (Porco et al., 2005). Furthermore this is a small object (3 km across, i.e., consistent with the ejecta sizes predicted by the models of Melosh, 1984); however, according to W. McKinnon (private communication), the surface of Mimas should be a poor source for ejecting large blocks of material. But, we believe, large fragments buried in the regolith might be better protected and more successfully launched than loose boulders sitting on the surface. We note that it is relatively easy to obtain orbits similar to that of

S/2004 S1 by ejecting material from Herschel: in our alternative runs we also obtained a few orbits similar to those of these survivors (six of the 9 survivors in the alternative run also had orbits similar to this new moon; see Table 8). See Fig. 17 for the orbital evolution of a spall that settled into an orbit similar to that of S/2004 S1; however, by extending the integrations we observed that this object actually hit Mimas at $t = 1155$ years after launch. Only one survivor (a spall) was still orbiting Saturn after 10,000 years; its elements then were $a = 198,516$ km; $e = 0.0373$; and $i = 2.2^\circ$; note, however, that the orbit of S/2004 S1 is more circular and has a smaller inclination than this survivor.

9. Discussion/conclusions

There are several known large impact basins on the icy moons of Saturn. Because of the weak gravity of these moons, substantial amounts of impact ejecta escape into orbit around Saturn (15 to 25%, depending on the satellite and/or crater; see Moore et al., 2004). We have generated initial conditions for four such large craters in the form of positions and velocities for the ejecta blocks; these initial conditions are consistent with currently understood cratering physics. If the surface ice is loosely consolidated, then the ejection speeds should follow the model of Housen et al. (1983; ‘rubble’ model); on the other hand, if the surface is strong, then the spallation model of Melosh (1984) should apply. The ejecta orbits were followed with the SWIFT-RMVS3 symplectic integrator of Levison and Duncan (1994). We took into account the gravitational perturbations of Saturn’s classical satellites. For integrations of ejecta from Tethys, we also included its co-orbitals Calypso and Telesto. In addition we took into account the perturbations due to Saturn’s oblateness as well as the gravitational perturbations due to the Sun. Our observations and conclusions are as follows.

- Qualitatively, both ejection models lead to similar conclusions. Most ejecta are swept up by the source satellite, although some do reach other moons after spending some time orbiting Saturn. For example, depending on the ejection model used, between 96% and 99% of the particles ejected from Herschel came back to Mimas. For particles ejected from Odysseus, between 82% and 89% came back to Tethys; for material ejected from Penelope, also located on Tethys but on the trailing side, between 93% and 96% came back. In the case of Tirawa (on the leading side of Rhea) between 91% and 96% of the material came back to Rhea. In a previous study (Alvarellos et al., 2002) we had found that only $\sim 71\%$ of ejecta from Ganymede that reach planetocentric orbits get reaccreted; it may be that ejecta is more widely scattered in the jovian system, where the satellites are much more massive (or the difference could perhaps just reflect the different initial conditions). In striking con-

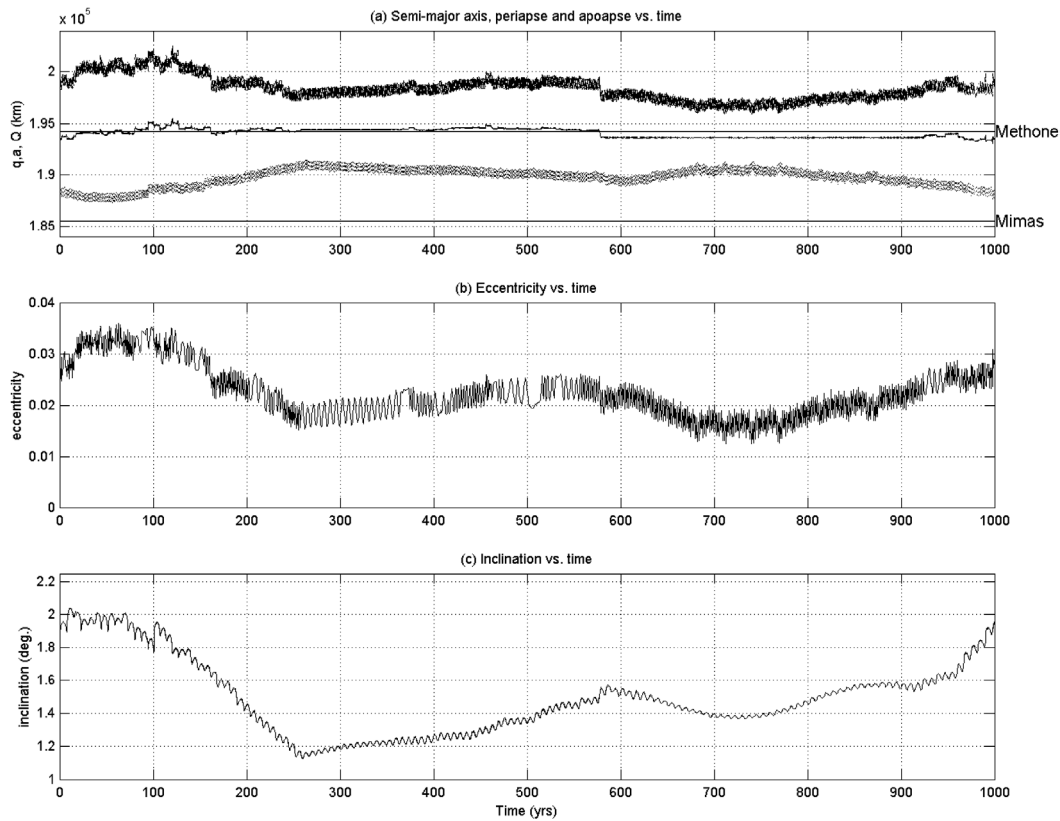


Fig. 17. Evolution of the orbital elements of a spall ejected from Herschel; this particular object went into an orbit that is very similar to that of S/2004 S1. (a) Semi-major axis a , periape distance q and apoapse distance Q as a function of time. Note that there are two periods of time ($260 < t < 360$, when $a \approx 1.944 \times 10^5$, and $590 < t < 930$, when $a \approx 1.9362 \times 10^5$) where the behavior is quite regular; the particle is not located in any obvious resonance during these times of seeming stability. The semi-major axis of Mimas is shown at the bottom of the plot as a horizontal line. (b) Eccentricity vs time. (c) Inclination (measured with respect to Saturn's equator) as a function of time; note that the inclination is quite regular during the interval $590 < t < 930$. Extending the integration past the nominal duration of 1000 years showed that this particle eventually hit Mimas at 1155 years.

trast, [Dobrovolskis and Lissauer \(2004\)](#) found that Hyperion reaccreted only $\sim 5\%$ of its own ejecta, while Titan accreted $\sim 78\%$; however, the dynamics in this case are qualitatively quite different, being strongly dominated by nearby massive Titan and its 4:3 mean-motion resonance with Hyperion itself. We also saw that while most Tethys ejecta are in principle able to reach the co-orbitals, in fact less than $\sim 0.1\%$ actually did so.

- Ejecta from the leading side of a moon (Herschel, Odysseus, Tirawa) tend to accrete on the trailing side of the source moon as the material gets swept up. In contrast, ejecta from the trailing side (i.e., Penelope) tend to accrete on the leading side of the source satellite.
- In addition to computing the initial conditions of the ejecta particles, we used Melosh's models ([1984](#)) to estimate the sizes of the ejecta blocks. Using impact velocities and block sizes of the ejecta we generate populations of 'poltorary' craters. The more conservative models suggest that poltorary craters of saturnian satellites should be rather small, typically on the order of 1 or 2 km in diameter. Only the more liberal spall model, in which tabular plates (spalls) remain more or less intact upon ejection predicts ~ 10 km diameter poltorary

craters; the biggest poltorary crater we have seen in this study is ~ 19 km in diameter. Larger poltorary craters would require: (a) Bigger ejecta blocks; this is unlikely, because the models we use assume maximum sizes. (b) Faster impact speeds than what we have seen (1.0 km/s for Rhea, 0.7 km/s for Tethys and 0.5 km/s for Herschel; see [Figs. 5, 9, 11, and 13](#)). One way to get this is to consider the possibility that at least some actual ejection speeds are faster than our models predict. We have neglected the near-field effects of the cratering process (jetting, etc.), which may produce hypervelocity ejecta. (c) Perhaps debris from large cratering events as we have studied here represents the low end tail of a putative planetocentric impactor population distribution. The high end tail of this distribution may be taken up by larger fragments resulting from catastrophic events of the type that can actually shatter moons (Hyperion, or the Ring parent body for instance; [Smith et al., 1981, 1982; Farinella et al., 1990](#); see [Dobrovolskis and Lissauer, 2004](#)). (d) The isotropically distributed craters on Mimas are primary craters as argued by [Lissauer et al. \(1988\)](#).

- The times to sweep up 50% of the debris span an order of magnitude in time, ranging from 10 years (Penelope ejecta, from Tethys) to 150 years (Tirawa spalls, from Rhea); see Fig. 6. These values are within an order of magnitude of the expected values given by Eq. (12), at which point the fractions of the original populations left range from 15 to 25%. We will deal with the statistical behavior of these ejecta swarms in more detail in a future paper.
- We also examined the behavior of the few particles which survived at the end of the integrations. It is relatively easy to inject debris from Herschel onto orbits similar to that of the newly discovered moon S/2004 S1 (‘Methone’), which raises the possibility that it was once a piece of Mimas itself. Note that if it is a spall, we would predict that S/2004 S1 should have a strongly tabular shape, like a ‘monolith.’ We believe that the surface of Enceladus could be a more likely source of spalls, although it would be more difficult to obtain a Methone-type orbit, as we would need a large impact basin on Enceladus’ trailing hemisphere. We also saw that it is difficult for impact debris from moons interior to Titan to reach heliocentric space. However, a few particles ejected from Rhea did escape from the Saturn system, while another few achieved high a , e , i orbits that show signs of long-term stability. We saw no hits on Saturn itself, in contrast to the system-wide scattering by Titan of ejecta from Hyperion found by Dobrovolskis and Lissauer (2004).

Acknowledgments

We acknowledge the following persons for useful discussions: H.J. Melosh, J. Lissauer, L. Dones, H. Levison, J. Burns, W. McKinnon, R. Olmstead, J.L. Alvarillos Sr., D. Stratemmeier, and C. Plescia. C. Chapman and B. Ivanov are gratefully acknowledged for their useful and insightful reviews. As always, the patience of my “pichus” is invaluable: Alejandra, Joselito, and Isabellita. This work has made use of NASA’s Astrophysics Data System (ADS located at <http://adswww.harvard.edu>) and was written using MiKTeX ver. 2.1. We thank the NASA Exobiology Program for support.

Appendix A. Ejection models

In this section we summarize the two ejection models used in this study: Spallation (due to Melosh, 1984, 1985a, 1989) and ‘Rubble’ [ejection speeds from Housen et al. (1983), and block sizes from Melosh (1984)]. The models are valid in the far-field regime, for which we expect directivity effects (i.e., ejecta preserving a ‘memory’ of the direction of projectile impact) to be small; this approximation

breaks down in the case of highly oblique impacts. Quantitative sample outputs from both models are shown in Table 4.

A.1. Spallation

Melosh (1984) approximates an impact by an underground explosion occurring at a point (the equivalent center) a depth δ below the surface

$$\delta = d(\rho_i/\rho_t)^{1/2}, \quad (\text{A.1})$$

where d is the impactor diameter and ρ_i and ρ_t are the impactor and target densities, respectively. Melosh (1984) gives two versions of his spallation model; we adopt his slightly more complicated but more realistic stress-wave model, rather than his hydrodynamic model.⁴ In the stress-wave model, a compressive wave originates from the equivalent center and propagates radially outward. Upon reaching the surface at a distance x from the impact point, this wave makes an angle θ with respect to the vertical ($\tan\theta = x/\delta$). Two waves are reflected back from the surface into the target: a tensile wave reflected at an angle θ and a shear wave reflected at an angle ϕ . The relationship between θ and ϕ is given by

$$\frac{\sin\phi}{\sin\theta} = \left(\frac{1-2\nu}{2-2\nu}\right)^{1/2}, \quad (\text{A.2})$$

where ν is the Poisson ratio⁵ of the target material. At the surface itself, the waves interfere destructively and zero pressure results. Pressure cancellation is progressively less efficient at greater depths; eventually this pressure becomes larger than the tensile strength of the target material and a spall breaks off the surface. The ejection speed v_e of this spall is given by the vector sum of the particle velocities in the three waves:

$$v_e = \frac{2v_p \sin\theta}{(\tan\phi \tan^2 2\phi + \tan\theta) \cos^2 2\phi}. \quad (\text{A.3})$$

Assuming a projectile impact speed U , Melosh (1984) gives the following expression for particle speed v_p :

$$v_p = \left(\frac{\rho_i}{\rho_t}\right) \left(\frac{U}{2}\right) \left(\frac{d}{2\sqrt{x^2 + \delta^2}}\right)^{1.87}. \quad (\text{A.4})$$

The thickness of the ejected spall layer z_s is given by Melosh’s (1984) complicated Eq. (27), which for the sake of brevity we do not reproduce here, but we note that in the stress-wave model z_s depends on a number of variables, including δ , and the tensile strength σ_t of the target material.

⁴ Melosh (1984) writes that the hydrodynamic ejection model uses the “theory of hydrodynamic stress waves to create a simple model of stress-wave fragmentation and ejection of target material.” A peculiarity of this model is that it predicts vertical ejection.

⁵ The Poisson ratio for a given material is defined as minus the ratio of the lateral strain to the axial strain in uniaxial stress; its value is 0.5 for an incompressible material.

Later, Melosh (1985a) approximated the spall thickness by

$$z'_s \approx \frac{\sigma_t d}{\rho_t C_L v_e}, \quad (\text{A.5})$$

where C_L is the P-wave (longitudinal) speed in the target material. Melosh (1984) estimated the maximum length l_s and width w of the ejected spalls as:

$$l_s = 1.09 \left(\frac{\sigma_t}{\sigma_r} \right) \frac{(x^2 + \delta^2)^{3/2}}{x \delta \sin \zeta}, \quad (\text{A.6})$$

$$w = \left(\frac{\sigma_t}{\sigma_r} \right) \frac{x(x^2 + \delta^2)^{1/2}}{\delta \sin \zeta}. \quad (\text{A.7})$$

Here ζ is the ejection angle measured from the local vertical. The quantity σ_r is the radial stress on the target material,

$$\sigma_r \approx \rho_t C_L v_p. \quad (\text{A.8})$$

The spall thickness z_s is typically about an order of magnitude smaller than either the spall width w or length l_s . One choice is to equate the volume of a spall $z_s l_s w$ to that of a sphere and from that define a mean spall diameter $\langle L \rangle = (6z_s l_s w / \pi)^{1/3}$, as was done by Vickery (1986); this sets an upper limit. On the other hand, one might reasonably question whether slabs ten times wider than they are thick could actually fly away intact. A second conservative option is to suppose that the slabs break into smaller pieces with the characteristic dimension being the spall thickness.

The stress-wave spallation model predicts that the ejection zenith angles should increase as a function of distance from the impact site. Since the surfaces of Saturn's satellites are mostly water ice (Chapman and McKinnon, 1986, p. 529), we approximate Melosh's (1984) ejection zenith angles ζ in degrees for an ice target (curve 7 of his Fig. 6) by

$$\zeta = 8x/d. \quad (\text{A.9})$$

The target material underneath the spall zone is not shielded from high pressures and therefore it is finely crushed and comminuted. Once the spall plates are ejected, the underlying material is exposed and ejected at speeds generally less than 1/3 of the particle speed v_p (Melosh, 1984, 1985a, 1985b). The characteristic size of these main excavation flow particles is about an order of magnitude smaller than z_s , as given by the Grady–Kipp relation (Melosh, 1984, 1985a). These smaller, slower-moving debris becomes the bulk of the ejecta blanket, but does not concern us further; we are interested in the bigger, higher-speed ejecta from near the surface.

A.2. Impacts on regolith: 'Rubble' model

For regolith in the gravity regime Housen et al. (1983) relate the ejecta speed v_e to the distance x from the impact site:

$$v_e = K \sqrt{g R_t} (x/R_t)^{-e_x}, \quad (\text{A.10})$$

where both K and e_x are constants, g is surface gravity and R_t is the transient crater radius [see also Chapman and McKinnon (1986, p. 516)].

There are several studies recommending various values for the constants e_x and K . Cintala et al. (1999) performed a series of experiments in which they shot aluminum spherules into coarse sand and found that the above equation fits their ejecta data very well; they find $1.52 < e_x < 2.01$. Melosh (1989) uses $1.8 < e_x < 2.4$ (p. 92; p. 124); Chapman and McKinnon (1986) use $1.52 < e_x < 2.50$. For specificity we adopt Zahnle et al.'s version (2003) of Schmidt and Housen's (1987) crater scaling, from which it follows that $e_x = 1.77$.

Regarding the constant K , Cintala et al. (1999) empirically find $0.336 < K < 0.490$. Melosh (1989, p. 92) gives $K = 0.39$; Chapman and McKinnon (1986) suggest a value close to unity. We adopt the convention that as x tends to R_t , v_e approaches the particle speed v_p [given by Eq. (A.4)]; assuming that $R_t^2 \gg \delta^2$, the constant K is then given by

$$K \approx 0.62 \left(\frac{\rho_i}{\rho_t} \right)^{0.2}. \quad (\text{A.11})$$

Cintala et al. (1999) also measured ejection angles and they found empirically that $34^\circ < \zeta < 54^\circ$, with a slight trend of increasing ζ as the crater rim is approached. However, since the Housen et al. model (1983) predict constant ejection angles, and in Alvarellos et al. (2002) we found that the fate of ejected particles is not a strong function of ejection angles, for simplicity we choose to set the zenith angle $\zeta = 45$ degrees for the rubble ejecta.

Housen et al.'s model does not predict ejecta sizes so for that we again turn to Melosh (1984). The maximum diameter of a rock on top of regolith which can be ejected intact as

$$l_r = \frac{d \sigma_c \sqrt{x^2 + \delta^2}}{4U \delta \rho_t v_p}, \quad (\text{A.12})$$

where σ_c is the crushing strength of the fragment.

References

- Alvarellos, J.L., Zahnle, K.J., Dobrovolskis, A.R., Hamill, P., 2002. Orbital evolution of impact ejecta from Ganymede. *Icarus* 160, 108–123.
- Bate, R., Muller, D., White, J., 1971. *Fundamentals of Astrodynamics*. Dover, New York.
- Batson, R.M., 1984. *Voyager 1 and 2 Atlas of Six Saturnian Satellites*. NASA SP-74.
- Bierhaus, E.B., Chapman, C.R., Merline, W.J., Brooks, S.M., Asphaug, E., 2001. Pwyll secondaries and other small craters on Europa. *Icarus* 153, 264–276.
- Burns, J.A., Gladman, B.J., 1998. Dynamically depleted zones for Cassini's safe passage beyond Saturn's rings. *Planet. Space Sci.* 46, 1401–1407.
- Chapman, C., McKinnon, W., 1986. Cratering of planetary satellites. In: Burns, J., Mathews, M.S. (Eds.), *Satellites*. Univ. of Arizona Press, Tucson, pp. 492–580.
- Cintala, M.J., Berthoud, L., Horz, F., 1999. Ejection–velocity distributions from impacts into coarse-grained sand. *Meteorit. Planet. Sci.* 34, 605–623.
- Dobrovolskis, A.R., Alvarellos, J.L., Zahnle, K., 2000. A dynamical survey of the jovian system. *Bull. Am. Astron. Soc.* 32. Abstract 1116.

- Dobrovolskis, A.R., Lissauer, J.J., 2004. The fate of ejecta from Hyperion. *Icarus* 169, 462–473.
- Duncan, M., Quinn, T., Tremaine, S., 1989. The long term evolution of orbits in the Solar System: A mapping approach. *Icarus* 82, 402–418.
- Farinella, P., Paolicchi, P., Strom, R.G., Kargel, J.S., Zappala, V., 1990. The fate of Hyperion's fragments. *Icarus* 83, 186–204.
- Gilbert, G.K., 1893. The Moon's face: A study of the origin of its features. *Bull. Phil. Soc. Washington* 12, 241–292.
- Gladman, B., 1993. Dynamics of systems of two close planets. *Icarus* 106, 247–263.
- Hamilton, D., Burns, J., 1994. Origin of Saturn's E-ring: Self-sustained, naturally. *Science* 264, 550–553.
- Harper, D., Taylor, D.B., 1993. The orbits of the major satellites of Saturn. *Astron. Astrophys.* 268, 326–349.
- Horedt, G.P., Neukum, G., 1984. Planetocentric versus heliocentric impacts in the jovian and saturnian satellite systems. *J. Geophys. Res.* 89, 10405–10410.
- Housen, K.R., Schmidt, R.M., Holsapple, K.A., 1983. Crater ejecta scaling laws: Fundamental forms based on dimensional analysis. *J. Geophys. Res.* 88, 2485–2499.
- Levison, H.F., Duncan, M.J., 1994. The long-term dynamical behavior of short period comets. *Icarus* 108, 18–36.
- Levison, H.F., Duncan, M.J., 1997. From the Kuiper Belt to Jupiter-family comets: The spatial distribution of ecliptic comets. *Icarus* 127, 13–32.
- Lissauer, J., Squyres, S.W., Hartmann, W.K., 1988. Bombardment history of the Saturn system. *J. Geophys. Res.* 93, 13776–13804.
- McGhee, C.A., Nicholson, P.D., French, R.G., Hall, K.J., 2001. HST observations of saturnian satellites during the 1995 ring plane crossings. *Icarus* 152, 282–315.
- Melosh, H.J., 1984. Impact ejection, spallation and the origin of meteorites. *Icarus* 59, 234–260.
- Melosh, H.J., 1985a. Ejection of rock fragments from planetary bodies. *Geology* 13, 144–148.
- Melosh, H.J., 1985b. Impact cratering mechanics: Relationship between the shock wave and excavation flow. *Icarus* 62, 339–343.
- Melosh, H.J., 1989. *Impact Cratering*. Oxford Univ. Press, New York.
- Moore, J.M., Schenk, P.M., Bruesch, L.S., Asphaug, E., McKinnon, W.B., 2004. Large impact features on middle-sized icy satellites. *Icarus* 171, 421–443.
- Morrison, D., Owen, T., Soderblom, L.A., 1986. The satellites of Saturn. In: Burns, J., Mathews, M.S. (Eds.), *Satellites*. Univ. of Arizona Press, Tucson, pp. 764–801.
- Murray, C.D., Dermott, S.F., 1999. *Solar System Dynamics*. Cambridge Univ. Press, New York.
- Porco, C.C., 34 colleagues, 2005. Cassini imaging science: Initial results on Saturn's rings and small satellites. *Science* 307, 1226–1236.
- Schmidt, R.M., Housen, K.R., 1987. Some recent advances in the scaling of impact and explosive cratering. *Int. J. Impact Eng.* 5, 543–560.
- Shoemaker, E.M., 1962. Interpretation of lunar craters. In: Kopal, Z. (Ed.), *Physics and Astronomy of the Moon*. Academic Press, New York, pp. 238–259.
- Shoemaker, E.M., Wolfe, R.F., 1982. Cratering time scales for the Galilean satellites. In: Morrison, D. (Ed.), *Satellites of Jupiter*. Univ. of Arizona Press, Tucson, pp. 277–339.
- Smith, B.A., 26 colleagues, 1981. Encounter with Saturn: Voyager 1 Imaging science results. *Science* 212, 163–191.
- Smith, B.A., 28 colleagues, 1982. A new look at the Saturn system: The Voyager 2 images. *Science* 215, 504–537.
- Smith, B.A., 32 colleagues, 1986. Voyager 2 in the uranian system: Imaging science results. *Science* 233, 43–64.
- Szebehely, V.G., 1967. *Theory of Orbits*. Academic Press, New York.
- Veverka, J., Thomas, P., Johnson, T.V., Matson, D., Housen, K., 1986. The physical characteristics of satellite surfaces. In: Burns, J., Mathews, M.S. (Eds.), *Satellites*. Univ. of Arizona Press, Tucson, pp. 342–402.
- Vickery, A.M., 1986. Size–velocity distribution of large ejecta fragments. *Icarus* 67, 224–236.
- Vickery, A.M., 1987. Variation in ejecta size with ejection velocity. *Geophys. Res. Lett.* 14, 726–729.
- Weissman, P.R., Dobrovolskis, A.R., Stern, S.A., 1989. Constraints on impact rates in the Pluto–Charon system and the population of the Kuiper Comet belt. *Geophys. Res. Lett.* 16, 1241–1244.
- Wisdom, J., Holman, M., 1991. Symplectic maps for the n -body problem. *Astron. J.* 102, 1528–1538.
- Zahnle, K., Dones, L., Levison, H.F., 1998. Cratering rates on the Galilean satellites. *Icarus* 136, 202–222.
- Zahnle, K., Schenk, P., Sobieszczyk, S., Dones, L., Levison, H.F., 2001. Differential cratering of synchronously rotating satellites by ecliptic comets. *Icarus* 153, 111–129.
- Zahnle, K., Schenk, P., Levison, H., Dones, L., 2003. Cratering rates in the outer Solar System. *Icarus* 163, 263–269.